UNIVERSITÀ
DI PAVIA

Dipartimento di Chimica
Direttore Ch.ma Prof. Antonella Profumo

Corso di Laurea Magistrale in Chimica

Synthesis and characterisation by Asymmetrical Flow Field Flow Fractionation (AF4) of Silver Nanoparticles with organic coatings

Sintesi e caratterizzazione mediante Asymmetrical Flow Field Flow Fractionation (AF4) di Nanoparticelle di Argento con rivestimenti organici

Relatore:
Ch.mo Prof. Yuri Antonio Diaz Fernandez

Correlatore:
Dott.ssa Enrica Alasonati
Dott.ssa Lavinia Rita Doveri

Tesi di Laurea di
Ester Cantoni

Anno Accademico 2023 / 2024

Index

Thesis Abstract

Synthesis and characterisation by Asymmetrical Flow Field Flow Fractionation (AF4) of Silver Nanoparticles with an organic coating;

Ester Cantoni.

Supervisor: Ch.mo Prof. Yuri Antonio Diaz Fernandez; Co-supervisors: Dottssa Enrica Alasonati; Dottssa Lavinia Rita Doveri

The aim of this thesis was the synthesis of silver nanoparticles of different sizes and their subsequent functionalisation with organic coatings. A second aim was the batch characterisation and monitoring of medium- to long-term stability of the particles, to be used in the development of fractionation protocols by means of Asymmerical Field Flow Fractionation. To achieve these aims, three synthesis procedures were used, including the $AgNO_3$ direct reduction, the seed-growth synthesis of larger particles, and the functionalisation of AgNPs with human serum albumin (HSA), bovine serum albumin (BSA), and various polyethelenglycol-thiolated molecules (SH-PEG750, SH-PEG5000-COOH, SH-PEG6000, SH-PEG10000, SH-PEG20000).

The characterisation techniques employed were UV-Vis spectroscopy for the determination of the optical properties of the particles; transmission electron microscopy to determine size and morphology of the particles, Dynamic Light Scattering for the determination of size, concentration, zeta potential and polydispersity of pristine and functionalised particles in colloidal solution. Asymmetrical Field Flow Fractionation was used for the fractionation of colloidal solutions of functionalised AgNPs, and for their online characterisation using various detectors (multiangle light scattering MALS, UV-Vis, differential refractive index dRI).

After different attempts, two reliable synthesis methods were developed providing two sets of particles with specific nominal sizes 40 and 80 nm, respectively, as confirmed by the size parameters determined by DLS and TEM. Functionalisation and subsequent characterisation of the coated particles confirmed the formation of a shell of organic material. Measurements at DLS, UV-Vis and TEM also established that the functionalisation step had no significant influence on the key properties of the AgNPs, except for the particle size, which increased to different extents, depending on the coating used. Stability monitoring also showed that all particles were stable up to 4 months after synthesis.

The development of the fractionation method using AF4 led to the definition of a system configuration and elution programme effective in fractionating particles of different sizes and with different coatings. Retention times and data obtained from the AF4-coupled detectors proved to be consistent with the characterisation of the particles in batch measurements.

Despite the results obtained in this thesis, some aspects remained to be clarified. One example is the anomalous behaviour of a particular set of particles (AgNP40_BSA) during fractionation at the AF4, and additional stability tests needed to ensure that the small fluctuations observed over time were not statistically significant. However, due to the robustness of the syntheses and their long-term stability, these silver particles have proven to be good candidates for the development of fractionation methods via AF4, paving the way for their future use as reference materials for calibration tests.

Riassunto breve della tesi

Sintesi e caratterizzazione mediante Asymmetrical Flow Field Flow Fractionation (AF4) di Nanoparticelle di Argento con rivestimento organico;

Ester Cantoni.

Relatore: Ch.mo Prof. Yuri Antonio Diaz Fernandez; Correlatore: Dottssa Enrica Alasonati; Dottssa Lavinia Rita Doveri

Questa tesi ha avuto come scopo la sintesi di nanoparticelle di argento di dimensione variabile e la loro successiva funzionalizzazione con rivestimenti organici. Un'ulteriore obiettivo è stato la loro caratterizzazione in batch ed il monitoraggio della loro stabilità a medio-lungo termine, ed infine il frazionamento mediante Asymmerical Flow Field Flow Fractionation. Per raggiungere questi scopi, è stato fatto uso di tre procedure di sintesi tra cui una riduzione di $AgNO_3$, una sintesi seed-growth ed una procedura di funzionalizzazione di AgNPs con proteine (albumina serica umana HSA, albumina serica bovina BSA) e vari molecole contenenti polietilenglicole-tiolati (SH-PEG750, SH-PEG5000-COOH, SH-PEG6000, SH-PEG10000, SH-PEG20000).

Le tecniche di caratterizzazione impiegate sono state la spettroscopia UV visibile (UV-Vis) per la determinazione delle proprietà ottiche delle particelle; la microscopia a transmissione elettronica (TEM) per la determinazione della dimensione e della morfologia delle particelle, il Dynamic Light Scattering per la determinazione del raggio idrodinamico, concentrazione, potenziale zeta e polidispersione delle particelle in soluzione, sia nude che funzionalizzate. La tecnica di Asymmetrical Flow Field Flow Fractionation è stata utilizzata per il frazionamento delle soluzioni colloidali di AgNPs funzionalizzate, e per la loro caratterizzazione online tramite i detector accoppiati (multi-angolo scattering della luce MALS, spettroscopia UV-Vis, e indice di refrazione differenziale dRI).

Dopo diversi tentativi, sono stati sviluppati metodi di sintesi affidabili che fornissero due set di particelle delle dimensioni nominali da 40 e 80 nm, come confermato dai parametri di dimensione determinati tramite DLS e TEM. La funzionalizzazione e la successiva caratterizzazione delle particelle rivestite da ogni coating hanno confermato l’avvenuta formazione di uno shell di materiale organico intorno al core d’argento metallico. Le misure di DLS, UV-Vis e TEM hanno inoltre stabilito che la funzionalizzazione non ha avuto particolare influenza sui parametri chiave che caratterizzano le AgNP, anche se le dimensioni delle particelle sono aumentate in misura variabile a seconda del cappante utilizzato. Il monitoraggio della stabilità ha inoltre attestato che tutte le particelle sono rimaste stabili fino 4 mesi dalla sintesi.

Lo sviluppo del metodo di frazionamento tramite AF4 ha portato ad un programma di eluizione efficace per frazionare le particelle di diverse dimensioni e con diverse ricoperture. I tempi di ritenzione e i dati ottenuti dai detector accoppiati all’AF4 si sono dimostrati in linea generale coerenti con la caratterizzazione delle particelle in batch.

Nonostante i risultati ottenuti in questa tesi, alcuni aspetti rimangono come domande aperte. Un esempio è il comportamento anomalo di un particolare set di particelle (AgNP40_BSA) durante il frazionamento all’AF4, o anche ulteriori test di stabilità per appurare se le piccole fluttuazione osservate nel tempo hanno significanza statistica. Tuttavia, grazie alla robustezza delle sintesi ed alla loro stabilità a lungo termine, le particelle di argento si sono dimostrate buoni candidati per lo sviluppo di metodi di frazionamento tramite AF4, aprendo la strada anche ad un loro possibile utilizzo come materiali di riferimento per test di calibrazione.

Riassunto esteso della tesi in lingua italiana

Si identificano con il termine “nanoparticelle” materiali che abbiano almeno una dimensione tra 1 e 100 nm.

Negli ultimi anni le nanotecnologie hanno conosciuto un enorme sviluppo che ne ha determinato l’impiego in moltissimi settori come quello farmaceutico, in nanomedicina, cosmetica, catalisi e molto altro.
Ciò è dovuto alle numerose proprietà che distinguono i nanomateriali dagli analoghi materiali bulk o dai singoli atomi, come ad esempio l’elevata energia superficiale, le proprietà ottiche singolari (ad es. la Localized Surface Plasmon Resonance) e quelle magnetiche, in particolare il superparamanetismo.
Moltissimi sono i metodi sviluppati per la loro sintesi, che si distinguono principalmente in due grandi categorie: sintesi bottom-up e sintesi top-down.
Una volta sintetizzate, le particelle nanometriche possono essere analizzate attraverso una varietà di tecniche di caratterizzazione (es DLS, spettroscopia UV-Vis, TEM, SEM).
Le nanoparticelle vengono distinte tipicamente in tre categorie, quelle basate sul carbonio, quelle organiche e quelle inorganiche.

In quest’ultima categoria rientrano le particelle metalliche di argento, AgNP, oggetto di studio di questa tesi.
Le NP di argento sono le particelle metalliche maggiormente impiegate negli ultimi anni, grazie alle loro proprietà antibatteriche.

Figura 1 *esempi di soluzioni colloidali commerciali di nanoparticelle di argento*

Ne è conseguita la proliferazione di metodi di sintesi che, sebbene si possano differenziare in metodi fisici, chimici e biochimici, si basano generalmente sullo stesso principio: la riduzione di un precursore metallico attraverso l'utilizzo di un agente riducente, e la successiva ricopertura della nanoparticella con un agente cappante per garantirne la stabilità in soluzione.

Nonostante le loro proprietà favorevoli, sono noti casi di tossicità delle AgNP, ad esempio a causa di rilascio di ioni Ag+ che possono intaccare organi come il fegato, i reni ed i polmoni.

D'altro canto, la grande stabilità di queste particelle può causarne il bioaccumulo con conseguenti incertezze riguardo i loro effetti sull'ambiente ed il loro destino a lungo termine.

Per questi motivi si è reso necessario sviluppare metodologie di caratterizzazione di NP che siano robuste ed affidabili.

Una tecnica che sta emergendo nell'ambito della caratterizzazione di soluzioni collodali di nanoparticelle di diversa natura è l'Asymetrical Flow Field Flow Fractionation (AF4).

Figura 2 *Immagine di un Sistema AF4 di Postnova*(13)

Si tratta di una tecnica di separazione la quale sfrutta il profilo parabolico che un flusso laminare assume quando attraversa uno stretto canale, per separare ed eluire a diversi tempi particelle di dimensioni diverse.

Facendo uso di una forza (chiamata Cross Flow) perpendicolare al flusso, le particelle vengono spinte contro una membrana permeabile al sovente ma non alle particelle degli analiti.

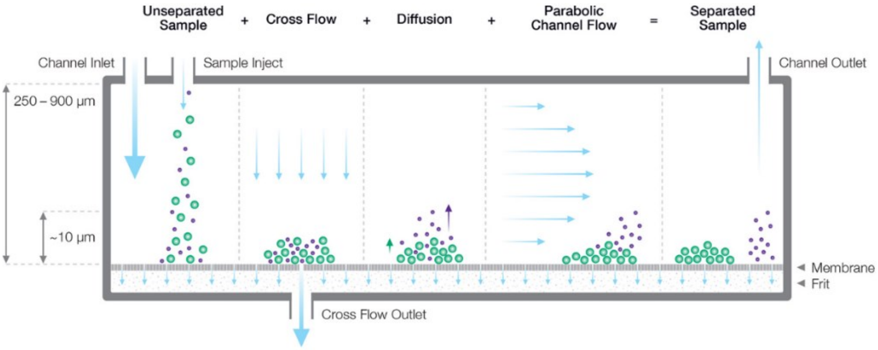

Figura 32 *Rappresentazione schematica di ciò che succede all'interno di un canale AF4 durante lo step di eluizione*(14)

Proporzionalmente alla loro dimensione, e quindi al diverso coefficiente di diffusione, le particelle diffondono lontano dalla membrana e si posizionano in sezioni del flusso a diversa velocità, facendo eluire per prime le particelle più piccole, e di seguito quelle via via più grandi.

Ciò viene espresso dall'Equazione 1 dove w indica lo spessore, η la viscosità dell'eluente, Vc la portata trasversale, k la costante di Boltzmann, A l'area della membrana porosa, T la temperatura assoluta e t° il tempo di vuoto del canale.(15)

$$d_H = \frac{2kTA}{\pi\eta V_c w t^0} t_r \qquad \text{[Eq. 1]}$$

Questo metodo è compatibile con matrici fisiologiche e consente di analizzare molti substrati grazie alla delicatezza della separazione, che non coinvolge interazioni con una fase stazionaria che potrebbero alterare il campione.

È possibile accoppiare l'AF4 a vari detector sia online (es MALS, UV-Vis) che offline (TEM, ICP-MS) per ottenere informazioni sulla dimensione, concentrazione ed altre proprietà delle particelle frazionate.

I principali obiettivi di questo lavoro sono stati i) la sintesi di nanoparticelle di argento di dimensione variabile e con diverse ricoperture organiche. ii) La loro caratterizzazione mediante DLS, UV-Vis, TEM ed il monitoraggio della loro stabilità a medio-lungo termine. Infine, iii) il frazionamento e la caratterizzazione delle AgNP attraverso l'uso di AF4 accoppiato ai detector MALS, UV-Vis e dRI.

La procedura di sintesi di AgNP di due diverse dimensioni (rispettivamente ca. 40 e 80 nm) è visibile nelle figure 4 e 5.

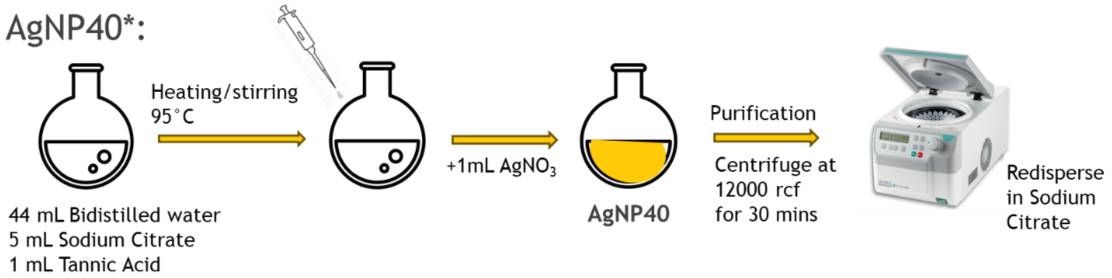

Figura 4 *Schema della procedura di sintesi per AgNP40*adattato da (17)*

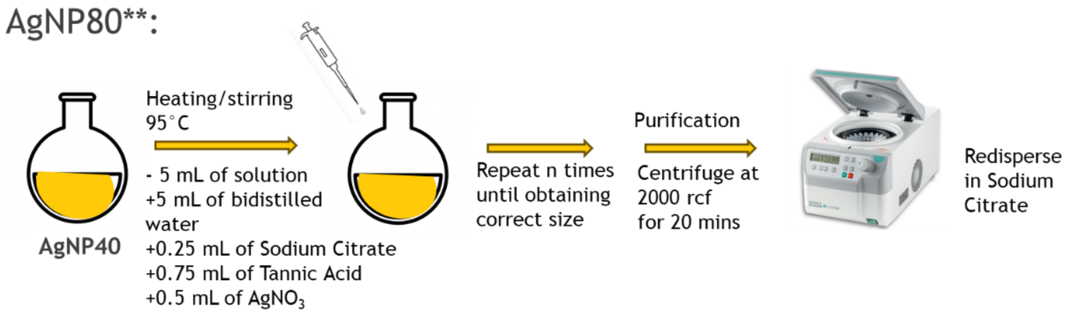

Figura 5 *Schema della procedura di sintesi per AgNP80 **Adattato da (18)*

Una volta sintetizzate e caratterizzate, le AgNP sono state funzionalizzate con sette diversi rivestimenti, tra cui due proteine (HSA e BSA) e cinque diversi PEG (PEG750, PEG5000COOH, PEG6000, PEG10000, PEG20000). La procedura di funzionalizzazione è visibile nella figura 6.

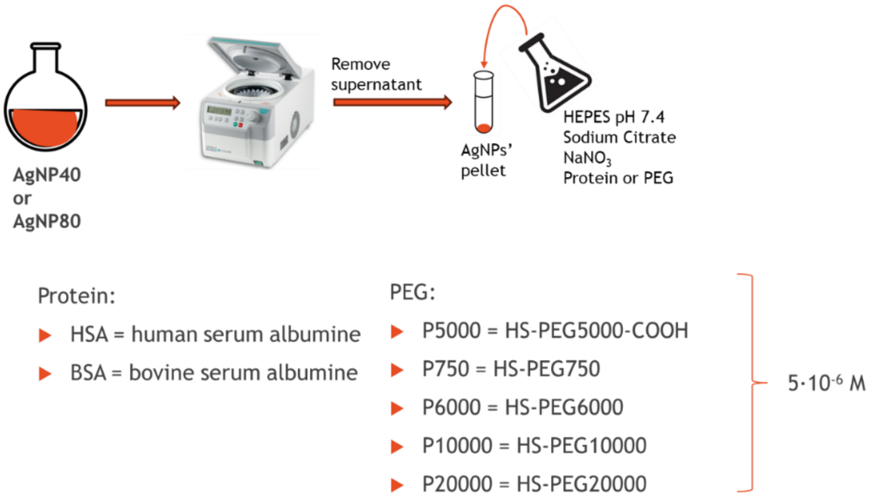

Figura 63 *Procedura di funzionalizzazione di AgNP40 e AgNP80 con 7 diversi agenti cappanti*

Risultati

La caratterizzazione di AgNP40 eAgNP80 ha compreso misure di DLS, UV-Vis e imaging TEM.

Le popolazioni di NP hanno mostrato una dimensione coerente con quanto atteso dalle procedure di sintesi, rispecchiate sia nei valori di dimensione ottenute al DLS sia nei valori di dimetro calcolati sulla base delle immagini TEM.

Gli indici di polidispersione acquisiti al DLS, la simmetria dei picchi UV e l'analisi visiva delle immagini TEM hanno dimostrato il carattere monodisperso delle soluzioni colloidali delle popolazioni di particelle di entrambe le dimensioni.

Infine il potenziale zeta negativo (Potenziale Zeta >|30| mV) ha garantito la stabilità in soluzione delle particelle.

Una volta funzionalizzate, le AgNP40 e le AgNP80 sono state sottoposte ad ulteriori caratterizzazione per verificare l'avvenuta funzionalizzazione, e gli effetti di quest'ultima sui parametri chiave che contraddistinguono le AgNP.

Sono stati analizzati 6 campioni, tra cui: AgNP40_HSA, AgNP40_BSA, AgNP40_P5000, AgNP80_HSA, AgNP80_BSA, AgNP80_P5000.

L'aumento di dimensioni atteso contestualmente alla formazione del guscio del rivestimento è stata dimostrata sia per le AgNP40 che per le AgNP80 funzionalizzate.

Infatti i valori di raggio misurati al DLS si sono tutti rivelati maggiori rispetto alle particelle non funzionalizzate, nonché gli spettri UV hanno mostrato uno spostamento verso il rosso della λ_{max} per tutti i campioni analizzati.

Ciò che è rimasto invariato invece sono le immagini TEM; infatti la funzionalizzazione era prevista formare un guscio organico sulla superficie della particella, non rilevabile con la microscopia elettronica a trasmissione standard.

Anche i valori di PDI non hanno mostrato significativi cambiamenti, rimanendo minori di 1 e confermando la presenza di soluzioni monodisperse.

Sebbene soggetti a delle diminuzioni rispetto alle particelle pure, tutti i potenziali zeta sono rimasti sufficientemente negativi da garantire la stabilità delle particelle in soluzione.

È stata anche portata avanti una prova di stabilità nel tempo, monitorando i parametri di dimensione e intensità normalizzata al MADLS, e di λ_{max} ed estinzione al massimo del picco all'UV-Vis.

I punti temporali stabiliti per la prova sono stati di due, quattro, ventiquattro ore e quattro mesi per le AgNP40 e AgNP80 funzionalizzate con HSA, BSA e P5000, ovvero gli agenti di rivestimento di maggiore interesse.

In generale, tutte le particelle hanno mostrato un andamento stabile della dimensione nel tempo, così come della lunghezza d'onda al massimo del picco, indicando un'assenza di aggregazione delle particelle.

Maggiore variabilità è stata riscontrata nell'andamento della intensità normalizzata all'angolo di 173° per le particelle AgNP80, indicando una possibile diminuzione della concentrazione delle particelle in soluzione.

Per queste particelle, anche l'estinzione alla lunghezza d'onda massima ha mostrato dei trend discordanti: una diminuzione del valore di estinzione per AgNP80_HSA probabilmente legato alla diminuzione della concentrazione di particelle in soluzione, ma anche il fenomeno opposto probabilmente (nel caso di AgNP80_BSA e AgNP80_P5000) dovuto all'evaporazione di solvente causata da un'inefficiente chiusura del contenitore.

Sebbene in diversi punti temporali (zero ore, ventiquattro ore, una settimana, quattro settimane), sono stati monitorati anche i campioni con i restanti rivestimenti: AgNP40_P750, AgNP40_P6000, AgNP40_P10000, AgNP40_P20000, AgNP80_P750, AgNP80_P6000, AgNP80_P10000, AgNP80_P20000.

Questi campioni hanno mostrato un comportamento simile ai campioni precedenti, mostrando la maggior stabilità nei valori di λ_{max}, e solo piccole variazioni nel caso di dimensioni, intensità normalizzata ed estinzione al massimo di assorbimento.

Queste fluttuazioni sulle proprietà delle AgNPs saranno analizzate più in dettaglio in un lavoro futuro. Tuttavia, per lo scopo di questa tesi, possiamo concludere che le particelle sono rimaste stabili nel tempo, aprendo alla possibilità di utilizzarle come materiali di calibrazione per lo sviluppo del metodo AF4 nella sezione seguente.

Le nanoparticelle d'argento di 40 e 80 nm rivestite con HSA, BSA e P5000 sono state scelte come campioni modello per sviluppare un metodo di frazionamento utilizzando il l’Asymmetrical Flow Field Flow Fractionation (AF4).

Il sistema utilizzato per l'analisi di queste NP comprendeva un canale standard e una membrana di cellulosa rigenerata con un cut-off del peso molecolare di 10kDa. Lo spaziatore aveva uno spessore di 350 µm e la fase eluente utilizzata è stata NovaChem® 0.125% v/v.

Sono stati testati vari programmi di eluizione.

Per primo un programma a Cross Flow costante di 0.1 mL/min, che ha però eluito il campione troppo presto. Successivamente è stato utilizzato un programma a gradiente lineare che ha spostato il picco a tempi di ritenzione maggiori fornendo tuttavia una peggior interpolazione dei dati MALS per il calcolo dell’Rms radius.

L’ultimo programma testato, che si è rivelato essere quello di maggior successo, è stato un gradiente esponenziale con un tasso di decadimento di 0.1.

Utilizzando questo metodo, sono stati analizzati due set di particelle di argento, differenti solo per dimensione: AgNP40_HSA e AgNP80_HSA.

Il tempo di ritenzione minore ottenuto per AgNP40_HSA ha confermato la loro inferiorità di taglia rispetto alle AgNP80_HSA, attestata anche dai valori di raggio ottenuti.

La strettezza e simmetria dei picchi UV, così come i valori di PDI ottenuti, hanno certificato la presenza di una popolazione monodispersa per AgNP40_HSA, mentre le AgNP80_HSA si sono rivelate più polidisperse.

I dati riportati in questa sezione hanno indicato che il metodo di gradiente esponenziale è stato efficace nel frazionare particelle in un'ampia gamma di dimensioni. Hanno inoltre sottolineato come questi materiali possono essere utilizzati per l'ottimizzazione di metodi AF4 e come potenziali materiali di riferimento per test di calibrazione per determinare la dimensione di nanoparticelle a partire dai tempi di ritenzione.

Le ultime analisi condotte hanno avuto lo scopo di confrontare l'effetto della funzionalizzazione delle AgNP sulla loro separazione in AF4. Per questo scopo sono stati analizzati tre set di particelle: AgNP40_HSA, AgNP40_BSA e AgNP40_P5000.

Queste particelle hanno mostrato picchi stretti a riprova del loro carattere monodisperso, e tempi di ritenzione in linea con i dati ottenuti al MADLS, per cui le particelle più grandi (AgNP40_HSA) hanno anche riportato il tempo di ritenzione maggiore.

Viceversa, si sono presentate delle anomalie nei valori di raggio ottenuti, che hanno rivelato un comportamento anomalo per AgNP40_BSA: infatti il valore di tempo di ritenzione e quello del raggio ottenuto al DLS e TEM provano che queste particelle siano più piccole di quelle di AgNP40_HSA. Tuttavia i valori di raggio ottenuti al MALS sono maggiori per le particelle rivestite con BSA invece che per quelle rivestite con HSA.

Dal momento che questo fenomeno non può essere razionalizzato sulla base dei dati disponibili, ulteriori esperimenti saranno pianificati come lavoro futuro per chiarire questa anomalia.

1. Introduction

1.1. Nanoparticles (NPs): their properties and applications

Nanoparticles (NPs) are materials with at least one dimension measuring between 1 and 100 nanometers. Their nanoscale size and high surface area confer unique physical and chemical properties different from bulk materials, making them ideal for numerous commercial and domestic applications. However, these particles are often highly stable and resistant to degradation, potentially causing environmental toxicity.(1)

There are different types of nanoparticles, e.g. carbon based, organic and inorganic NPs that can be based on metals or metal oxides.

In this work we focused on hybrid core-shell nanoparticles with an inorganic core and an organic coating at the surface.

Nanomaterials can exhibit various morphologies and shapes, for example spherical, cylindrical, tubular, star-shaped, prism-shaped. Moreover they are typically classified into four categories based on the number of dimensions that are under 100 nm (Figure 1) namely 0D, 1D, 2D, or 3D.(2)

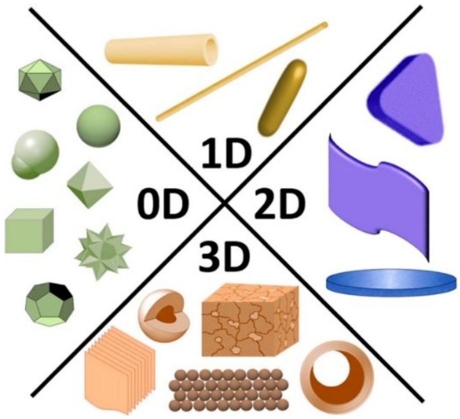

Figure 4 *Schematic representation of different morphologies of nanomaterials. 0D nanomaterials have all dimensions in the nanoscale. 1D and 2D nanomaterials have one and two dimensions, respectively, beyond the nanoscale. 3D nanomaterials are microstructures with nanofeatures, such as hollow microstructures with nanoshells and nanoparticle-based micro assemblies*(3)

1.1.1. NP synthesis methods

Nanoparticles are synthesized using various methods categorized into bottom-up or top-down approaches. A simplified representation of these processes is shown in **Errore. L'origine riferimento non è stata trovata.**.

The bottom-up or constructive method involves the building of materials from atoms to clusters to nanoparticles. Common bottom-up techniques include sol-gel, electrospinning, chemical vapor deposition (CVD), pyrolysis, and biosynthesis.

The top-down or destructive method involves breaking down bulk materials into nanometric scale particles. Widely used top-down techniques include mechanical milling, nanolithography, laser ablation, sputtering, and thermal decomposition.(2)

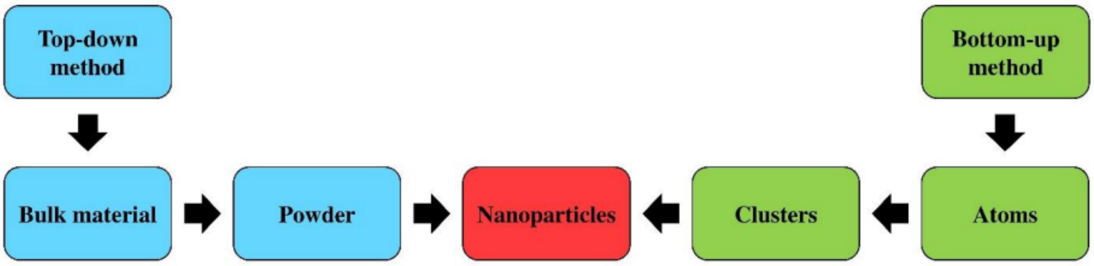

Figure 5 Top-down and bottom-up NPs synthesis methods(2)

1.1.2. NP characterisation techniques

Different characterisation techniques can be employed for the analysis of key physicochemical properties of NPs (**Errore. L'origine riferimento non è stata trovata.**). These include techniques such as UV-Vis spectroscopy to determine optical properties, Transmission Electron Microscopy (TEM) to establish highresolution morphology, structural integrity and coating uniformity, SEM-EDX for the elemental analysis and the investigation of variability in chemical composition and Dynamic Light Scattering (DLS) to assess the hydrodynamic radius, NPs number concentration as well as stability in biological matrices.

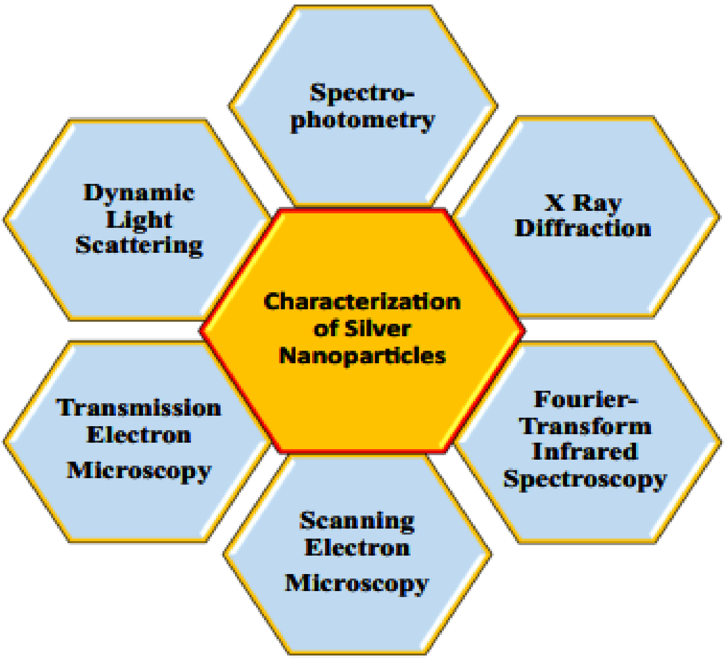

Figure 6 *Different techniques used for the characterisation of NP* [(4)]

1.1.3. NP key properties

Different physicochemical properties of NPs are related to their small size and differentiate nanomaterials from bulk materials and single atoms or molecules. A key characteristic of NPs is the high surface energy resulting from the large number of surface atoms, which are highly energetic. In nanoparticles, the surface area to volume ratio is, in fact, very large.

This high surface energy results in significant reactivity, causing nanoparticles to reduce their energy by aggregating, adsorbing chemical species, or dispersing into ions by oxidation.

Another notable feature of NPs is their optical properties. In fact, noble metal nanoparticles display size-dependent optical properties and strong UV-visible extinction bands that are absent in the bulk metal spectrum. This phenomenon is attributed to localized surface plasmon resonance.(1)

Localized surface plasmons (LSPs) (**Errore. L'origine riferimento non è stata trovata.**) are due to oscillations of charge density confined within metallic nanoparticles by the effect of external electromagnetic fields. When LSPs are excited by an electromagnetic wave of light at a resonant incident wavelength, a strong light scattering is observed, with the consequent appearance of an intense surface plasmon extinction bands. The frequency (extinction maxima) and intensity of the LSP absorption bands are distinctive to the type of material and are highly influenced by the size, size distribution, and shape of the nanostructures, as well as the optical properties of their surrounding environment, including the substrate, solvents, and adsorbates.(5)

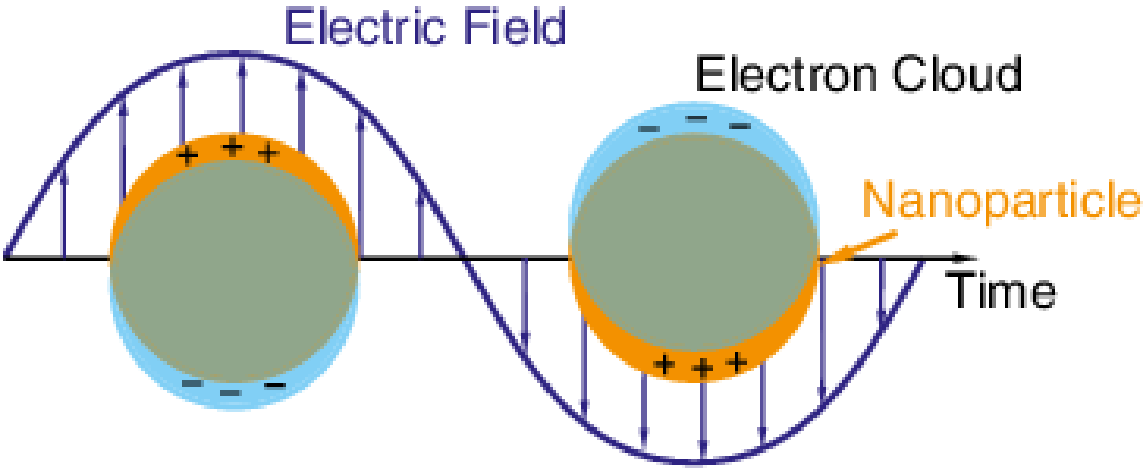

***Figure 7** Schematic representation of localized surface plasmon resonance effect (LSPR (6)*

Lastly, many metallic nanoparticles exhibit magnetic properties distinct from their bulk counterparts, particularly being superparamagnetic. Superparamagnetism refers to the capacity of a single-domain ferromagnetic particle to become magnetized at elevated temperatures when exposed to an external magnetic field and to lose this magnetization entirely once the magnetic field is removed (no permanent magnetization).(7)

Due to all these characteristics, NPs are suitable candidates for various commercial and domestic applications, which include catalysis, bioimaging, medical coatings, energy-based research, and environmental applications. For example, iron oxide nanoparticles such as magnetite (Fe3O4) or its oxidized form maghemite (Fe_2O_3) are used for efficient contrast for imaging applications in Magnetic Resonance analysis as well as for photo thermal therapeutic applications.(8)

Another important application is the use of platinum nanoparticles in the automotive catalytic converters as they reduce the amount of platinum required due to very high surface area of the nanoparticles thus improving performance while reducing significantly the cost of the catalyst. Some chemical reactions for example, reduction of nickel oxide to metal nickel (Ni) are performed using nanoparticles.(2)

The use of nanoparticles in sunscreen can also provide numerous advantages such as the UV protection property of titanium oxide and zinc oxide nanoparticles as they are transparent to visible light and can absorb and reflect UV rays. Some lipsticks also use iron oxide nanoparticles as a pigment.(9)

1.2. Silver nanoparticles

In recent years, the powerful antibacterial properties of engineered silver nanoparticles (AgNPs) have led to a great increase in their use.

***Figure 8** Examples of commercial colloidal soultions of silver nanoparticles*

They are one of the most extensively metal NPs produced and have been applied in various areas such as optical biosensor, pollutant remediation, electronics, household, plastic additives, cosmetics, and health care products.

This widespread and often indiscriminate use of nano-silver is inevitably increasing the probability that such materials can be accidentally or deliberately dispersed into the environment. Once present in the environment the normally useful antibacterial properties of the silver may instead become a potential hazard to human health, agriculture and wildlife. (10)

1.2.1. AgNPs synthesis procedures

Various synthesis methods for AgNPs exist nowadays, and can be classified in (i) chemical, (ii) physical and (iii) biological methods (

Figure **9** Schematic representation of possible AgNPs synthesis methods. Adapted from (1, 11)

).

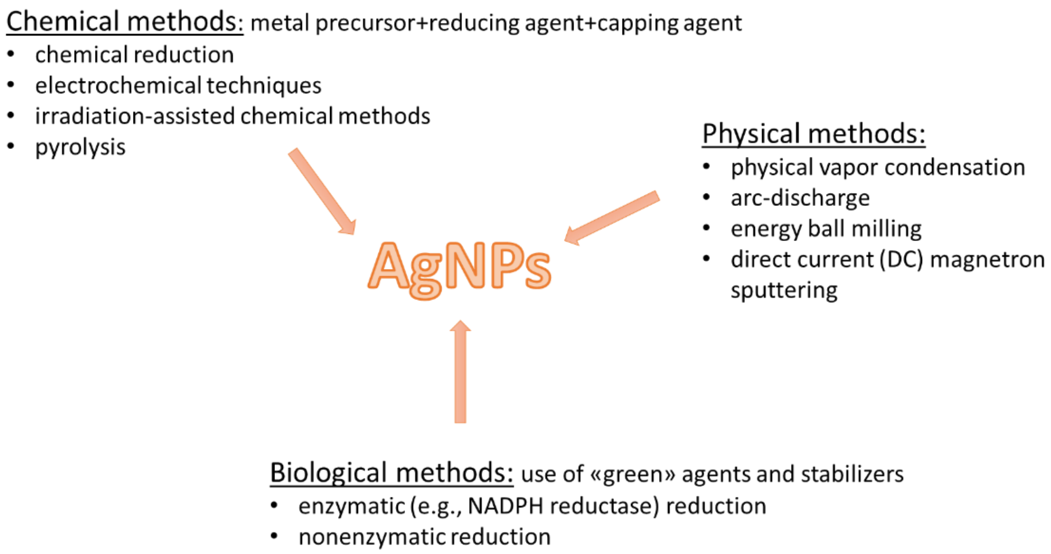

Figure 9 *Schematic representation of possible AgNPs synthesis methods. Adapted from (1, 11)*

Examples of chemical methods for synthesizing silver nanostructures are chemical reduction, electrochemical techniques, irradiation-assisted chemical methods, and pyrolysis. Typically, the synthesis of silver nanoparticles in solution involves three main components: a metal precursor (for example Ag_2SO_4, AgO3), a reducing agent and a stabilizing or capping agent.

Typical capping agents are thiols, sodium citrate, polymers such as PVA (polyvinyl alcohol) and PVP (polyvinyl pyrrolidone).

Commonly used reducing agents for chemical synthesis methods include borohydride, sodium citrate, ascorbic acid, alcohols and hydrazine compounds.

Chemical methods are preferred for applications where accurate control over surface chemistry and dispersion of the nanomaterials in liquid media are required.

Physical methods, which do not involve toxic chemicals and usually offer fast processing times, include physical vapor condensation, arc-discharge, energy ball milling, and direct current (DC) magnetron sputtering. A significant advantage of physical methods is that the resulting silver nanoparticles have a narrow size distribution, yet the starting “dry” format of the nanomaterials may not be compatible with liquid dispersions.

In biological synthesis of AgNPs, toxic reducing agents and stabilizers are replaced by biomolecules such as proteins, carbohydrates, and antioxidants produced by living organisms, including bacteria, fungi, yeasts, and plants. The possible mechanisms for biological synthesis include enzymatic (e.g., NADPH reductase) and nonenzymatic reduction.(11) Controlling purity and surface chemistry is not often simple in biological synthesis methods, due to the presence of complex matrices during the synthesis.

1.2.2. AgNPs main features

The physicochemical properties of AgNPs, including size, shape, surface area, charge and surface coating, agglomeration and dissolution rate, are of significant importance in determining their chemical interactions and biological effects. The smaller the particle, the larger the surface area, which consequently increases the toxic potential.

The toxicity of AgNPs on humans, particularly those below 10 nm, is primarily due to the release of silver ions, with the liver being the primary target organ, followed by the spleen, lungs, and kidneys. When released into the environment, AgNPs are likely to react with sulfide, chloride, or other natural compounds, which can alter their original properties.(11)

Recent studies have examined the potential risks and mechanisms of silver nanoparticles (AgNPs) on microorganisms, identifying the generation of reactive oxygen species and Ag^+ ions as the primary sources of their toxicity. Factors such as the type and concentration of AgNPs, along with environmental properties like pH value, temperature, chemical composition, and concentrations at specific locations, can affect their stability, transport and distribution in the environment. These factors, in turn, influence the toxicity and bioavailability of AgNPs in aqueous environments.

The exceptional optical properties of silver nanostructures arise from their unique interaction with light, leading to the collective coherent oscillation of their free conduction band electrons, known as localized surface plasmon resonance (LSPR). The LSPR of AgNPs is influenced by their size, shape, dielectric environment, and mutual electromagnetic interactions among nearby particles. These factors can be adjusted to tune the plasmon peak of AgNPs within the ranges of 393–738 nm. Consequently, the LSPR of AgNPs results in strong visible and near-infrared (NIR) scattering and absorption, facilitating the development of photothermal and thermolytic laser therapies.(12)

Furthermore, AgNPs demonstrate a strong affinity for sulfur, a highly prevalent element in commonly utilized capping agents such as thiol-polyethylene glycol and proteins. This renders them an excellent model system for investigating the behaviour of NPs within a physiological matrix and the formation of a protein corona on the surface of the particles.

1.2.3. AgNPs applications

The exceptionally potent broad-spectrum antimicrobial activity of AgNPs drives the development of various AgNPs products, such as textiles, food storage containers, antiseptic sprays, catheters, and bandages. They are also being explored for therapeutic uses as antiviral and anticancer agents. Applications of silver nanoparticles are presented in **Errore. L'origine riferimento non è stata trovata.**.(11)

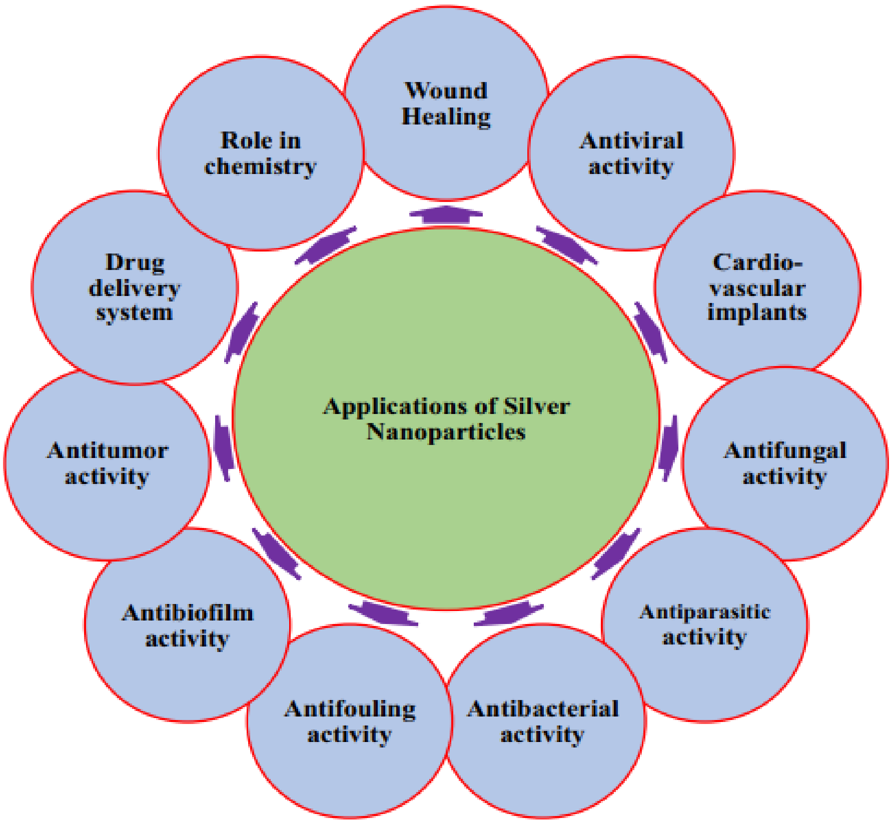

Figure 10 *Current and potential applications for silver nanoparticles*(4)

1.3. Multi detector Asymmetrical Flow Field Flow Fractionation

1.3.1. Asymmetrical Flow Field Flow Fractionation (AF4)

AF4 can be used to separate solutions of macromolecules and nanoparticles in the size interval from a few nm to the µm range. The first AF4 system was presented in 1987 by Giddings and Wahlund. In AF4 the separation is carried out in a thin ribbon-like channel between porous and nonporous plates. This separation technique exploits the fact that when a laminar flow runs through a thin channel, it assumes a parabolic profile, which means that the flow velocity is highest in the centre of the channel and zero at the walls.

By taking advantage of a force (called the Cross Flow or X-Flow) perpendicular to the channel flow, particles are pushed so to arrange themselves in different layers within the channel depending on their size. In this way, they are eluted from the channel output with different velocities.

Figure 11 *Image of a Postnova AF4 system*(13)

The channel is composed of different layers (Figure 9). Inside the channel, a membrane allows the carrier liquid to exit through the bottom channel wall and retains the analyte. This semi-permeable membrane, usually made of regenerated cellulose or polyether sulfone and called “accumulation wall”, is one of the critic parameters for AF4 separation. The membrane pore size, expressed as molecular weight cut-off, typically ranges from 1 kDa to 100 kDa.

As can be seen in Figure 9, the membrane is supported by a frit, which is encapsulated in the ground plate. Above the membrane is located a spacer made up of a polymer film with a typical thickness of approximately 100-500 µm, and above all an impermeable cover plate closes the channel.

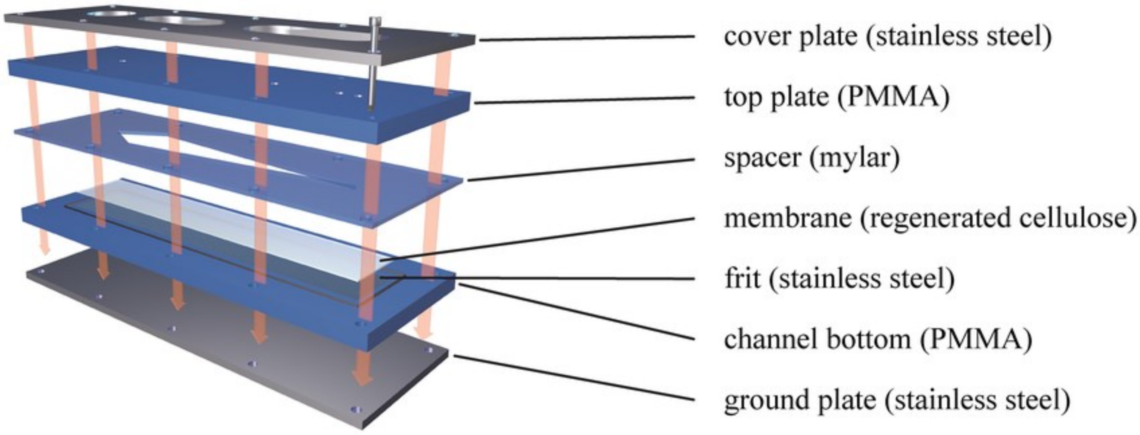

***Figure 12** Schematic representations of all the layers constituting the AF4 channel(13)*

As particles elute downstream, the Cross Flow pushes them towards the membrane. On the other hand, particles can diffuse back into the channel. The smaller the particles are the higher is the diffusion caused by their Brownian motion and the further the particles will diffuse back into the channel. As a result of these two opposite phenomena, differently sized particles become localized at different positions within the channel's parabolic flow profile, each at a different average distance from the membrane (called the mean layer thickness). This causes different populations of particles to be displaced downstream at a velocity equal to the mean parabolic flow at that position, hence smaller particles will elute before larger ones (Figure 10).

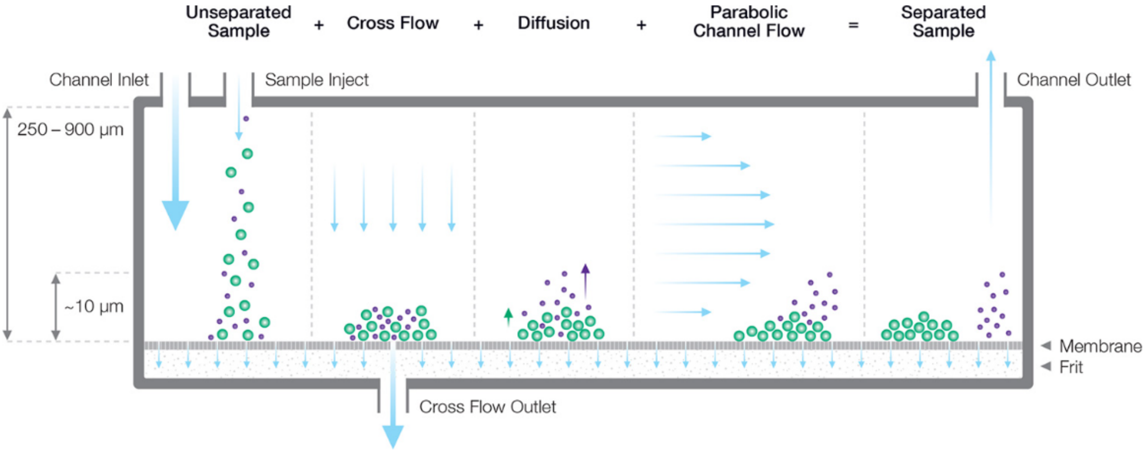

Figure 13 *Schematic representation of the happening inside the AF4 channel during the elution step*$^{(14)}$

The separation process requires three steps.

1. During **injection** the sample is carried from the loop in which it is injected to the inside of the channel.
2. After that, the **focusing phase** takes place, during which three flow rates are active: the tip flow rate, enters from the top carrying the sample with the chosen eluent and pushes it downstream to the detectors; the focus flow rate enters from about halfway up the membrane and is used in this phase as a flow opposite to the tip one, in order to focus all the incoming sample in a thin band in the beginning of the channel; and the cross flow rate, which is the driving field, used to push the nanoparticles towards the membrane.
3. Finally, in the **elution phase,** the focus flow is switched off and the sample is eluted to the outlet of the channel, while the cross flow rate continues to regulate the separation.

The hydrodynamic diameter d_H of the particles is related to the retention time t_r by Eq.1.

$$d_H = \frac{2kTA}{\pi\eta V_c w t^0} t_r \qquad \text{[Eq.1]}$$

where w is the channel thickness, η the eluent viscosity, V_c the cross flow rate, k the Boltzmann constant, A the porous membrane area, T the absolute temperature and $t°$ the channel void time.(15)

AF4 is a widely used separation technique thanks to the softness of the separation process, since it does not involve a stationary phase that can interact with, degrade or alter the sample. It can be employed for the analysis of colloidal systems such as liposomes, nanoparticles, polymers and virus-like particles, both in aqueous solutions or even in physiological matrices.

These reasons, other than the wide separation range that can be achieved (from a few nanometres to several micrometres), make it the ideal technique to be used for the analysis of pharmaceutical and nanomedicine products.

AF4 can be coupled with downstream online detectors such as UV-Vis, differential refractive index (dRI) and light scattering (static -MALS- or dynamic -DLS-) detectors and also with offline detectors such as TEM, SEM, ICP-MS to determine various sample’s features.

The two following paragraphs cover a description of MALS and dRI, two commonly used detectors coupled online with AF4; these have been used to carry on the analyses described in section 3.4.

1.3.2. Multi-angle light scattering (MALS)

A multi-angle light scattering (MALS) detector measures the static light scattered from a sample at multiple angles at the same time (**Errore. L'origine riferimento non è stata trovata.**). This allows to obtain the values of some key parameters as the absolute molecular weight (Mw) and the radius of gyration (Rg) of a sample.

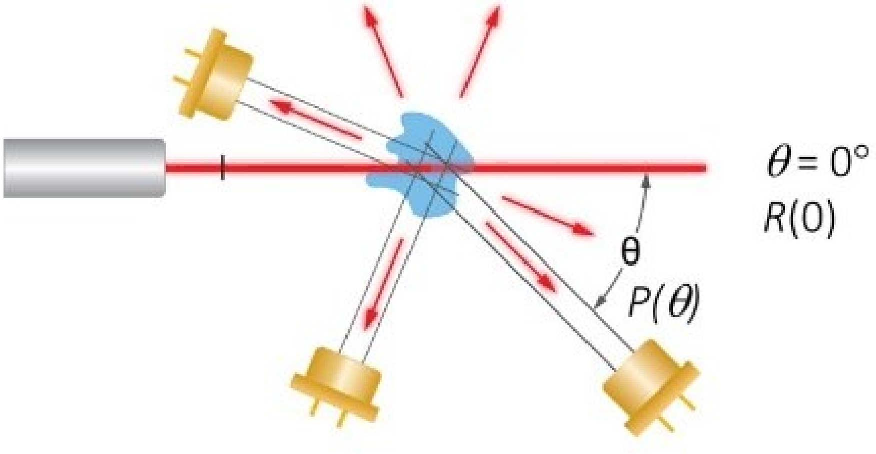

Figure 14 *Schematic representation of light diffusion from a sample inside MALS instrument*(16)

As long as the particle's size is negligible compared to the λ of the incident light (R<10 nm for a λ=660 nm), the intensity of the scattered light is directly proportional to the molar mass, to the concentration and to the refractive index increment *dn/dc* of the particle, which represents the change in refractive index (dn) of the solution per unit concentration (dc) of the solute. This is because the particle is very small and acts as an isotropic source of scattered light.

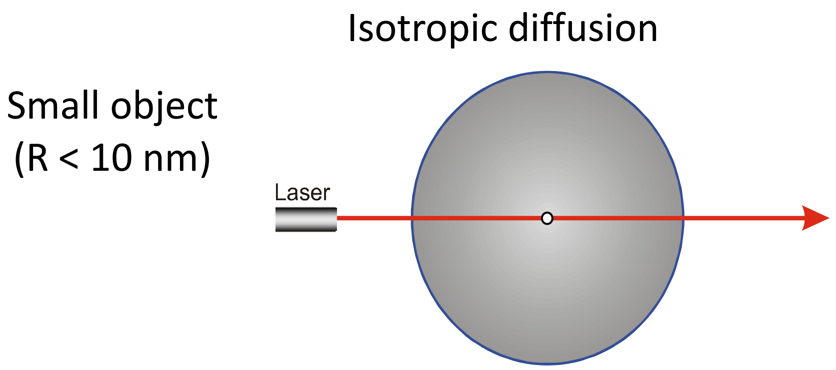

***Figure 15** Schematic representation of isotropic diffusion originating from a small object*(16)

However as the particle size increases, it becomes necessary to keep into account the effects of intramolecular interference. Because of these, the scattered signal starts to depend also on the angle in the plane perpendicular to the polarisation. At an angle of zero degrees, there is no attenuation of the scattered intensity (destructive interference), whilst as the angle increases, so does the attenuation. Eq.2 shows how the intensity of the scattered signal is directly proportional to the product of the molar mass of the particles, its concentration, and the angle of observation θ.

$$I(\theta)_{scattered} \propto Mc\left(\frac{dn}{dc}\right)^2 P(\theta)$$ [Eq.2]

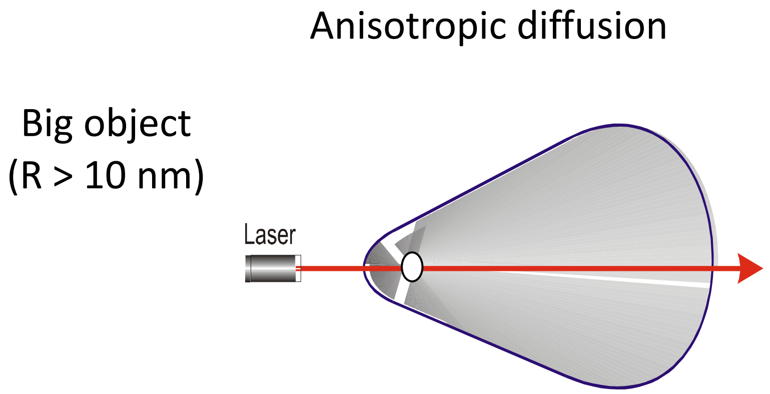

***Figure 16** Schematic representation of anisotropic diffusion originating from a big object*(16)

To determine the size of the particles, it is necessary to simplify the calculations. Large particles can be approximated as having many isotropic scattering centres. By integrating the phase shift of each of these scattering centres so to determine the degree of destructive interference, it is possible to calculate the total amount of light scattered at each angle.

As a result of this integration, the final equation contains an integral over the mass distribution of the large particle. This term is the root mean square radius (r_g) also called the radius of gyration. It is the mass distribution relative to the mass barycentre, weighted by the square of the distance to the barycentre (r_j) (Eq.3 and 4).

$$\langle r_j^2 \rangle = \frac{\sum r_j^2 m_j}{\sum m_j} \qquad \text{[Eq.3]}$$

$$r_g = \sqrt{\langle r_j^2 \rangle} \qquad \text{[Eq.4]}$$

The Z-average of the Rms radius (R_z in Astra software's report) is accurate whatever the molecular conformation (no concentration detector is needed).(16) This is because the software allows to fit data from MALS measurements with different models, and each of these models illustrates different conformations by using different form factors P(θ).

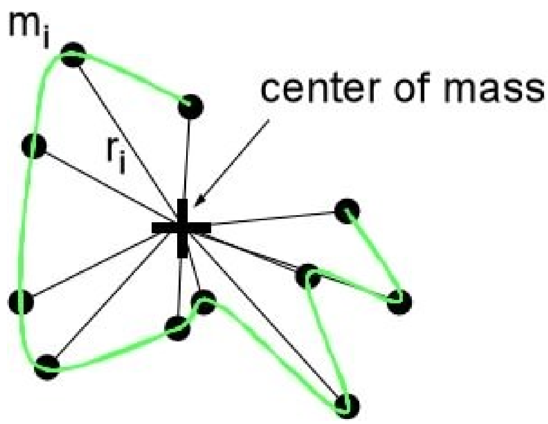

***Figure 17** Schematic representation of the distribution of masses relative to the centre of mass in a sample*[16]

1.3.3. Differential Refractive Index Detector (dRI)

The Refractive Index Detector is used for the analysis and quantification of components with limited or no UV absorption, such as alcohols, sugars, saccharides, fatty acids and polymers. **Errore. L'origine riferimento non è stata trovata.** represents the optical system of the instrument.

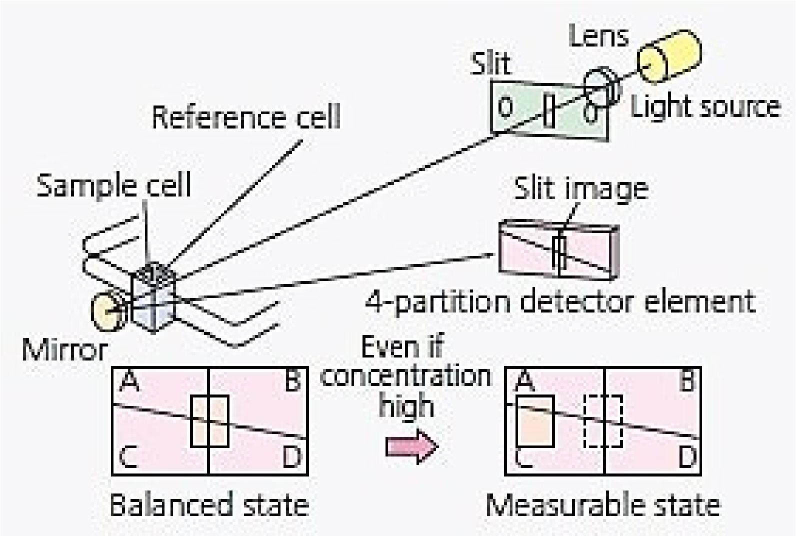

***Figure 18** Schematic representation of the optical system of a RI detector*

The light emitted from the lamp passes through the slit, and then through the flow cell as a parallel beam. The light is then reflected by the mirror, passes through the flow cell again, and a slit image is formed on the photodiode. The photodiode is divided in four parts for different purposes. In the high sensitivity analysis, the left and right parts are treated as one light receiving element, respectively.

The flow cell consists of two parts, the sample side and the reference side. When the refractive index of the cell in the sample side changes, the slit image formed on the photodiode moves horizontally in proportion to the difference in refractive index.

The difference in refractive index (Δn) is measured based on the variation in light intensity between left (A) and right (B) parts.

$$RI \div \frac{(A-B)}{(A+B)} \qquad \text{[Eq.6]}$$

Knowing the dn/dc value relative to the sample detected and the difference in refractive index (Δn), it is possible to obtain the concentration of the sample using Eq.7.

$$c = \frac{\Delta n}{dn/dc} \qquad \text{[Eq.7]}$$

1.4. Thesis Objectives

The scope of the work presented in this thesis was to synthesise and characterise silver nanoparticles of different sizes, functionalised with a range of organic coatings.

The use of silver nanoparticles (AgNPs) as antibacterial materials has increased in recent years. Consequently, these NPs were selected as a model system to investigate their behaviour in simulated physiological environments.

The first objective of the thesis was to develop a robust and reliable synthesis procedure to obtain silver nanoparticles of a desired sizes, adapting a method already published.

At the second stage, we focused on the functionalisation of the AgNPs surface with different coatings mimicking/simulating the protein corona that would form on the particle surface after contact with a physiological environment.

The coated particles were characterised and their stability was assessed over time, using complementary analytical techniques such as UV-Vis spectroscopy, DLS and TEM.

Finally, we developed a reliable analytical method for the separation of polydispersed colloidal solutions of AgNPs and for their determination in complex matrices by using Asymmetrical Flow Field Flow Fractionation (AF4) techniques.(10)

2. Experimental section

2.1. Materials

Silver Nitrate ($AgNO_3$, Sigma-Aldrich)
Tannic Acid (TA, Sigma-Aldrich)
Sodium Citrate (Na_3Ct, Sigma-Aldrich)
HEPES (Sigma-Aldrich)
Human Serum Albumin (HSA, Sigma-Aldrich)
Bovine Serum Albumin (BSA, Sigma-Aldrich)
Carboxylated Polyethilene Glycole 5000 (HS-PEG5000-COOH, Sigma-Aldrich)
Polyethilene Glycole 750 (HS-PEG750, Sigma-Aldrich)
Polyethilene Glycole 6000 (HS-PEG6000, Sigma-Aldrich)
Polyethilene Glycole 10000 (HS-PEG10000, Sigma-Aldrich)
Polyethilene Glycole 20000 (HS-PEG20000, Sigma-Aldrich)
NovaChem© (NC, 0.0125% v/v)
Hellmanex© (0.1% v/v)

H_2O is always to be intended as double-distilled (UniPV) or mQ (LNE) water when referring to AF4 carriers and sample dilutions. Double-distilled water was also used for synthesis, purification and functionalization steps.

2.2. Methods

2.2.1. Glassware pre-treatment

All the glassware used in the syntheses was pre-treated with aqua regia for 15 minutes and then washed three times with double-distilled water in an ultrasound bath for 5 minutes.

2.2.2. AgNP40 synthesis procedure

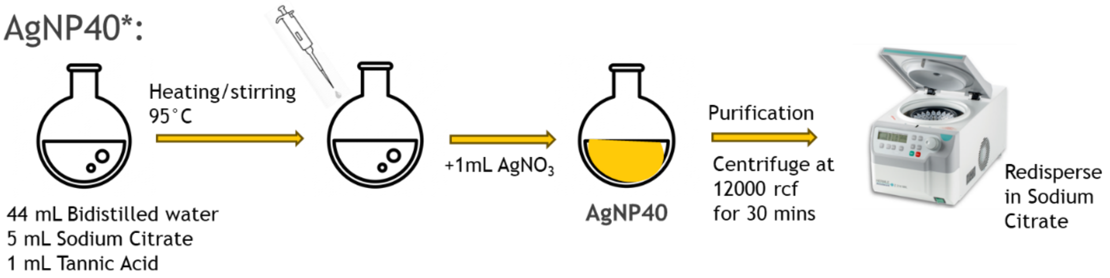

***Figure 19** Scheme of the synthesis procedure for AgNP40 *Adapted from* (17)

AgNP40 were synthesised using a reduction of $AgNO_3$ by tannic acid and were capped with citrate.

Using double-distilled water, the following aqueous solutions were prepared: tannic acid 50 mM (0.4252 g in 5 mL of H_2O), sodium citrate 50 mM (0.7353 g in 50 mL of H_2O) and $AgNO_3$ 25 mM (0.0425 g in 10 mL of H_2O).
After that, in a round bottom flask were added in order: 44 mL of double-distilled water, 5 mL of the sodium citrate solution and 1 mL of the tannic acid solution.
After 20 minutes of pre-heating, the flask was placed in the heating mantle and let heating and stirring until reaching 90-95°C.

Once reached this temperature, 1 mL of the $AgNO_3$ solution was added in a slow and continuous fashion, placing the tip end just above the liquid's surface.

The formation of AgNP40 was confirmed by the change in colour from yellow to amber.

The solution was left stirring for one more minute then the flask was removed from the mantle and let cool down.

It was then centrifuged at 12000 rcf for 20 minutes in order to remove the excess of reactants.

The supernatant was removed and the pellet containing the nanoparticles formed was dispersed in sodium citrate 2.2 mM, in a volume equal to the one of supernatant removed.

2.2.3. AgNP80 synthesis procedure

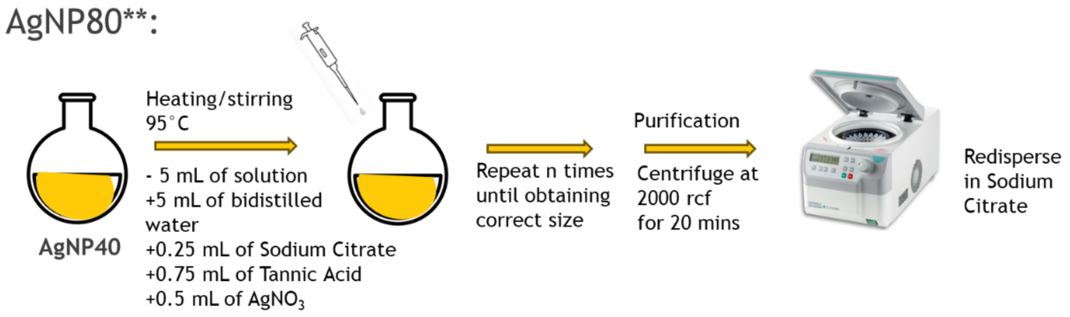

Figure 20 *Scheme of the synthesis procedure for AgNP80 **Adapted from*$^{(18)}$

AgNP80 were synthesised using a ''seed growth'' synthesis using AgNP40 as seeds.

The same procedure as above was performed until the addition of $AgNO_3$ and the consequent change of colour.

At this point the flask was kept on the heating mantle at 90°C and subsequent additions of reactants were performed every 25 minutes until reaching the desired size on NPs.

In this case, it was decided empirically that 8 additions were needed to obtain AgNPs of around 80 nm.

For the first addition, 9.75 mL of solution were removed, and then were to be added to the flask: 8.25 mL of H_2O, 250 µL of sodium citrate 25 mM, 750 µL of tannic acid 2.5 mM and 500 µL of $AgNO_3$ 25 mM.

The following additions were performed in the same way, except for the volume of solution removed (5 mL instead of 9.75 mL) and the volume of water added (5 mL instead of 8.25 mL).

After the 8th addition, the flask was taken out from the mantle and let cool down. The solution was then centrifuged at 2000 rpm for 30 minutes to remove the excess of reactants.

The supernatant was wiped off and the pellet containing the nanoparticles formed was dispersed in sodium citrate 2.2 mM, in a volume equal to the one of supernatant removed.

2.2.4. Functionalisation procedure

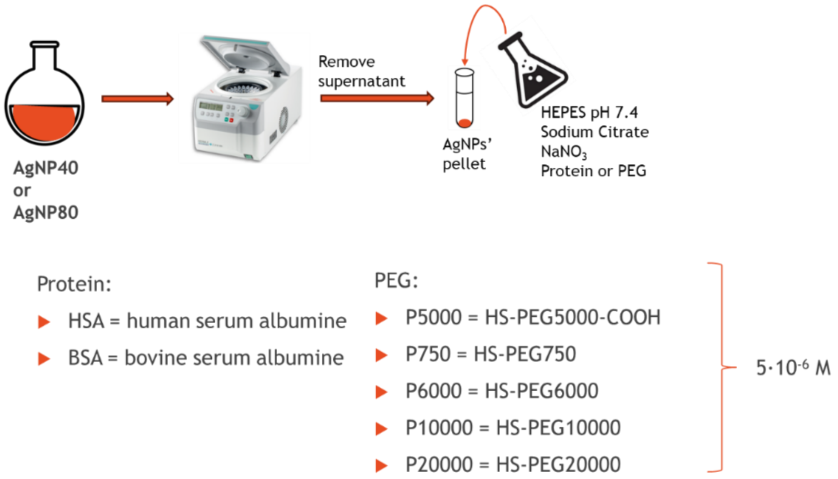

Figure 21 *Functionalisation procedure with 7 different coatings on AgNP40 and AgNP80*

Seven solutions were prepared dissolving a protein (HSA and BSA) or PEG (P750, P5000, P6000, P10000, P20000) in a HEPES buffer.

Separately, a solution of HEPES buffer 10 mM was made, with the addition of sodium citrate 2.2 mM and $NaNO_3$ 0.156 mM, and the pH was adjusted at 7.4 using NaOH.

After that, 100 µL of protein or PEG solution was added to 14.5 mL of the buffer to obtain a solution of protein or PEG which was $5 \cdot 10^{-6}$ M in the buffer.

Meanwhile, 15 mL of the colloidal solution of AgNPs were centrifuged and the supernatant was removed.

The remaining 400 µL of pellet were redispersed in the 14.6 mL of buffer containing the coater molecule and in this way 15 mL of functionalised AgNPs were obtained.

2.3. Instruments

2.3.1. UNIPV

UV-vis spectrophotometer (Varian Cary 6000, Agilent)

Multi Angle Dynamic Light Scattering (Zetasizer Nano ZS90, Malvern)

Transmission Electron Microscopy (JEM-1200 EX II 140, Jeol)

2.3.2. LNE Paris

AF4 (AF2000 MultiFlow FFF, Postnova)

UV-vis spectrophotometer (SPD-20A, Shimadzu)

MALS (Dawn Helios II, Wyatt Technologies)

dRI (RID-20A, Shimadzu)

ASTRA software (Version 6.1.7.17)

AF2000 software (Version 2.0.1.5)

2.4. Characterisation

2.4.1. Sample preparation

Dilutions were performed in double-distilled water.

After their synthesis (see section 2.2.2 and 2.2.3), AgNPs pristine were centrifuged and the pellet was redispersed in a solution of sodium citrate 2.2 mM. This solution was then diluted in double-distilled water, in a ratio accordingly to the characterisation performed.

As for functionalised AgNPs, the functionalisation procedure (see section 2.2.4) led them to being dispersed in a buffer solution. This solution of AgNPs was then diluted in double-distilled water to operate the measurements.

2.4.2. UV-Vis characterisation

Solutions of AgNP40 and AgNP80 were diluted 1:10 in 1 mL of H_2O. The range of wavelength set for the measurement went from 300 nm to 1100 nm, and the cuvette used was made of optical glass with an optical path of 1 cm.

2.4.3. MADLS characterisation

Solutions of AgNP40 were diluted 1:10 in 1 mL of H_2O.

Solutions of AgNP80 were diluted 1:60 in 1 mL of H_2O.

The cuvette used was made in plastic with an optical path of 1 cm, making sure it was well cleaned.

The measurements were performed at 25°C, at three different angles: the forward angle (13°), the 90° angle and the backscatter angle (173°).

The main measurements performed were Multi-Angle Dynamic Light Scattering (MADLS) Analysis, Particle concentration analysis and the determination of Zeta Potential.

2.4.4. TEM characterisation

AgNP40 and AgNP80 were diluted 1:10 in H_2O, placed on a copper TEM grid covered in collodion and let dry for one day.
Images were registered with a magnification of 40k, 60k and 75k with acceleration voltage 100 kV on the TEM instrument JEM-1200 EX II 140 from Jeol.

2.4.5. AF4 characterisation

Analyses on AF4 were performed using a standard channel, a regenerated cellulose membrane with a molecular cut-off of 10kDa. The spacer was 350 µm thick and the eluent used was NovaChem 0.0125% v/v in mQ water.

This AF4 was coupled online with a UV-Vis detector, a MALS detector and a dRI detector.

2.4.6. ASTRA software

This software was used for the elaboration of raw data collected from the different detectors coupled to AF4. ASTRA allowed to calculate the gyration radius distribution and averaged values. The software apply different procedures: band broadening, for correcting effects of fluid mixing between instruments, the alignment, for determining the interdetector delay, and normalisation for relating detector signals to the 90 degree detector signal and the instrument calibration constant. Moreover, it is possible to set the baselines, the analytical window and the best model for the fitting of the MALS data so to obtain a report containing all values of radius and related uncertainty.

3. Results and discussion

3.1. Synthesis, functionalisation and characterisation of silver nanoparticles

3.1.1. Characterisation of pristine AgNPs

Two different sizes of silver nanoparticles (AgNP40, size around 40nm and AgNP80, size around 80nm) were synthesized following the procedure described in section 2.2.2 and 2.2.3 (fig.16 and 17). In detail, AgNP40 were prepared with a one-pot synthesis methods while AgNP80 were obtained following a “seed-growth” procedure using AgNP40 as starting seeds.

After synthesis, both types of AgNPs were centrifuged to remove the excess of tannic acid and then characterized by means of multi-angle dynamic light scattering (MADLS), UV-Vis spectroscopy and transmission electron microscopy (TEM).

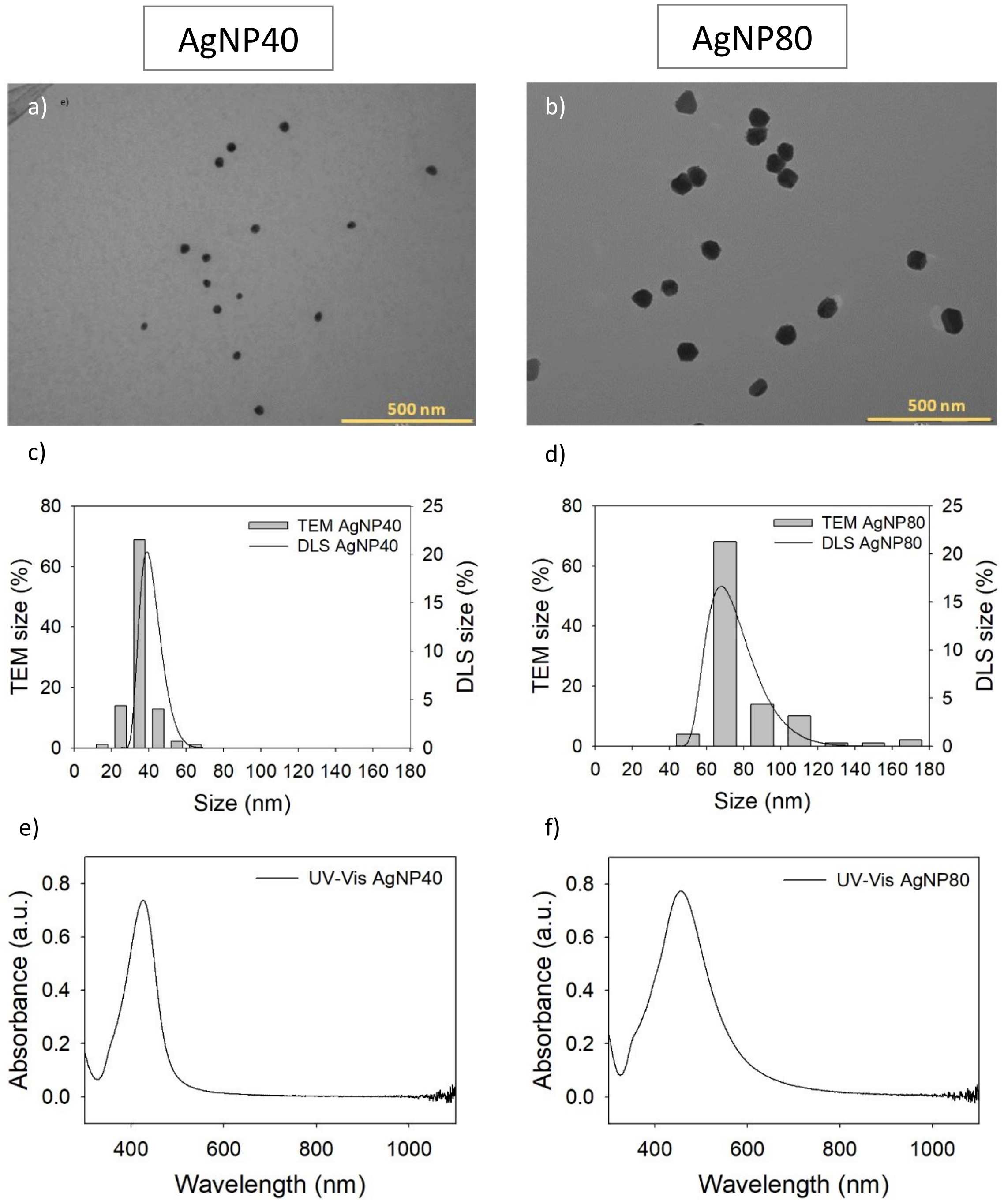

***Figure 22** General characterisation of AgNP40 and AgNP80; a) representative TEM image of AgNP40; b) representative TEM image of AgNP80; c) representative size distribution in diameter of AgNP40 from TEM* images (bars) and MADLS size distribution in number (plot); e) representative UV-Vis spectra of AgNP40; f) representative UV-Vis spectra of AgNP80. *Diameter calculated over 100 particles; magnification 75k*

***Table 1** UV-Vis, TEM and DLS data of AgNP40 and AgNP80*

Sample	***AgNP40 pristine***	***AgNP80 pristine***
λ_{max} (nm)	425	458
Extinction*	7.38	11.60
Size TEM§ (nm)	33 (±11)	78 (±13)
Z average (nm)	62 (±9)	79 (±4)
Size in intensityˆ (nm)	55.3 (±0.9)	97 (±3)
Size in numberˆ (nm)	35 (±2)	40 (±20)
Pdiˆ	0.20 (±0.02)	0.18 (±0.01)
Normalized intensityˆ (kcps) $\cdot 10^2$	393 (±8)	1180 (±7)
Particles concentration* (particles/mL) $\cdot 10^{10}$	11 (±4)	6 (±3)
Zeta potential (mV)	-46 (±2)	-48 (±2)

**Corrected for the dilution factor*

§Diameter and std dev calculated over 100 particles

ˆDetermined at the backscatter angle (173°)

Each value is the average of three repeats. Values are reported as mean (±std dev)

AgNP40 UV-Vis spectra showed a peak (fig.1e, f) reaching the maximum intensity at $\lambda_{max} \approx 425$ nm, while AgNP80 λ_{max} was attested to be at 458 nm (tab.1), showing an expected redshift due to the bigger particle size. The extinction values at optical path 1cm were 7.38 for AgNP40 and 11.60 for AgNP80. Typical UV-Vis peaks for both NP types resulted to be relatively narrow and symmetrical (fig.19e, f).

Follow up characterisation using TEM allowed the determination of the size of the nanoparticles. AgNP40s and AgNP80s resulted monodisperse with a quasi-spherical shape, as displayed in the TEM images reported in figure 1a, b.

Table 1 reports the average value of diameter calculated over 100 particles, leading 33 (±11) nm for AgNP40 and 78 (±13) nm for AgNP80, respectively.

These values were compared to the size values obtained by MADLS measurements, that proved to be higher. In fact, TEM images reveal the size of the particle core, whereas DLS measurements provide the hydrodynamic diameter, which is expected to be larger due to the layer of solvent molecules and capping ions attached to the particles.

As for MADLS measurements (tab.1), both the Z average and peak size in number and intensity measured at a 173° gave reasonable results compared to the ones expected from the synthesis procedure described in section 2.2.2 and 2.2.3.

AgNP40s and AgNP80s were confirmed as monodispersed with low polydispersity index (PDI, <0.5). This parameter measures the dispersion of the size distribution in the sample. Using MADLS (Malvern Zetasizer DLS), it was also possible to determine the particle concentration giving values in the order of magnitude of 10^{10} particles/mL. The Zeta potential of AgNP40s and AgNP80s is strongly negative (-46 (±2) and -48 (±2) mV), ensuring the stability in colloidal solution for both sets of AgNPs.

3.2. Characterisation of functionalised AgNPs

At a second stage, both AgNP40 and AgNP80 were separately functionalised with 7 different coatings, following a full combinatorial scheme presented in figure 18 (and described in section 2.2.4), namely two model proteins (HSA and BSA) and five different polyethylene glycol of specific chain lengths (P750, P5000COOH, P6000, P10000, P20000). This approach produced 14 different types of samples, covering the full combinatorial matrix of two AgNP types and seven capping agents.

Following a preliminary characterization, we selected three capping agents (HSA, BSA and P5000COOH) as the most suitable to be used as reference test samples to develop fractionation methods using the AF4 technique.

Furthermore, in this shortlist we included HSA as the most abundant protein in human plasma, and for comparison choose also BSA.

This choice was also supported by the need to have particles negatively charged at physiologcal pH that would be repulsed away from the AF4 regenerated cellulose membrane, a prerequisite for using this analytical technique without the aid of stabilizing surfactants. Following the rational of negative particle charge, we also selected the only PEG capping molecule with a carboxylate moiety.

On the samples coated with these three capping agents, a more intensive characterisation of AgNPs was carried out, including TEM imaging and stability assessment up to four months.

Additionally, key characteristics of AgNPs functionalised with the other coating agents were also assessed, including colloidal stability over time.

AgNP40

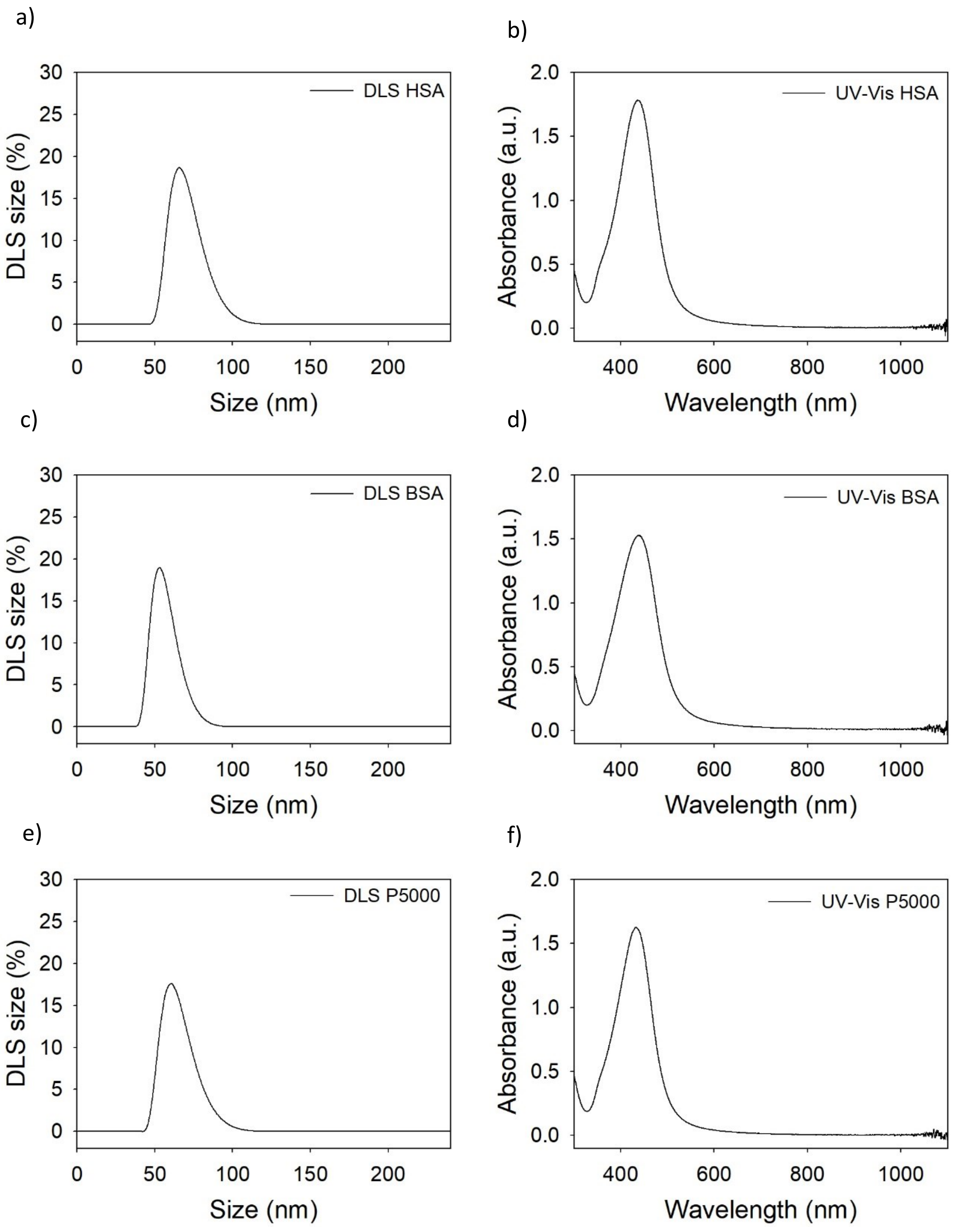

Figure 23 *General characterisation of AgNP40 with different coatings a) representative MADLS size distribution in number of AgNP40_HSA; b) representative UV-Vis spectra of AgNP40_HSA; c) representative MADLS size distribution in number of AgNP40_BSA; d) represent representative UV-Vis spectra of AgNP40_BSA; e) representative MADLS size distribution in number of AgNP40_P5000; f) representative UV-Vis spectra of AgNP40_P5000*

AgNP80

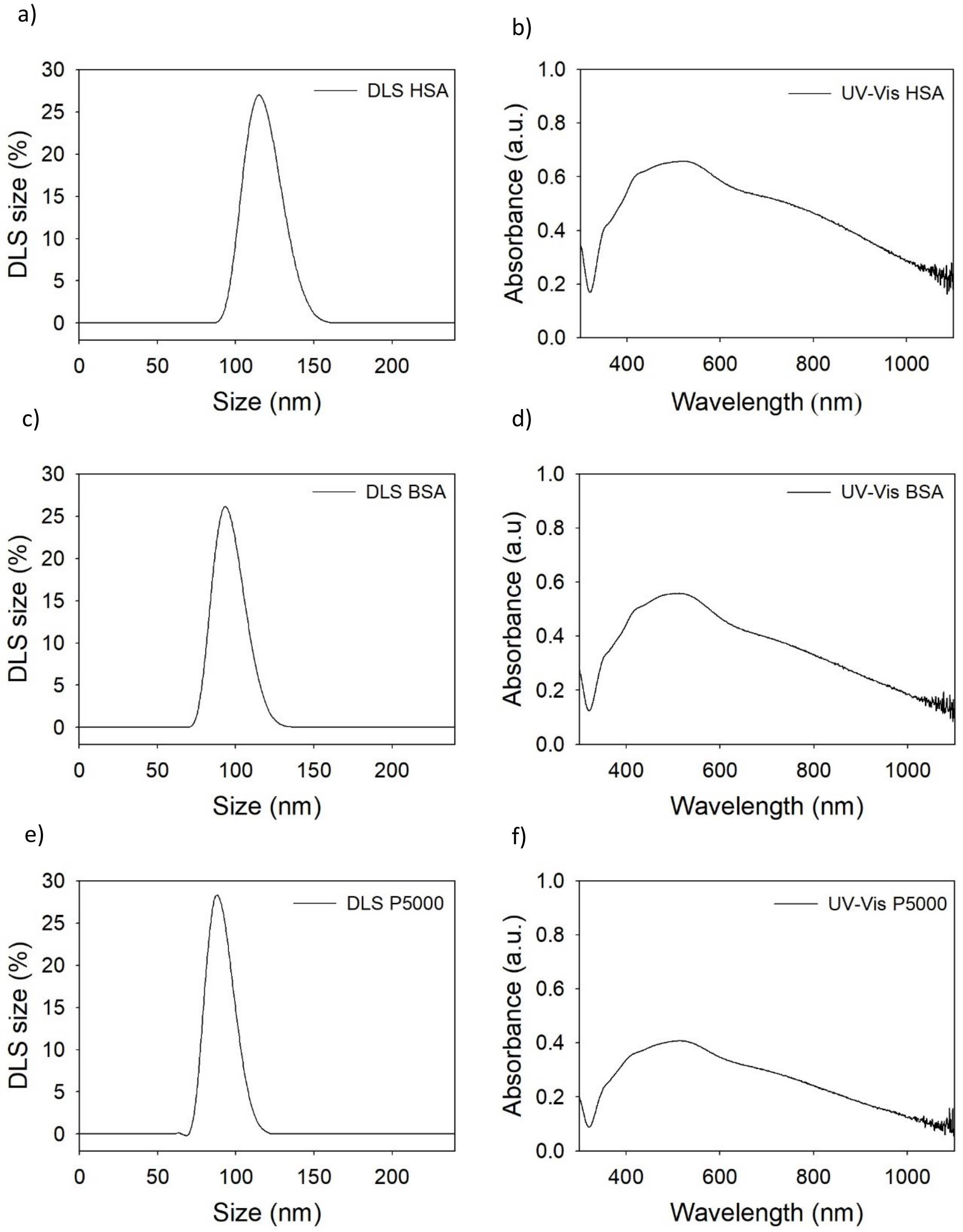

Figure 24 *General characterisation of AgNP80 with different coatings a) representative MADLS size distribution in number of AgNP80_HSA; b) representative UV-Vis spectra of AgNP80_HSA; c) representative MADLS size distribution in number of AgNP80_BSA; d) representative UV-Vis spectra of AgNP80_BSA; e) representative MADLS size distribution in number of AgNP80_P5000; f) representative UV-Vis spectra of AgNP80_P5000*

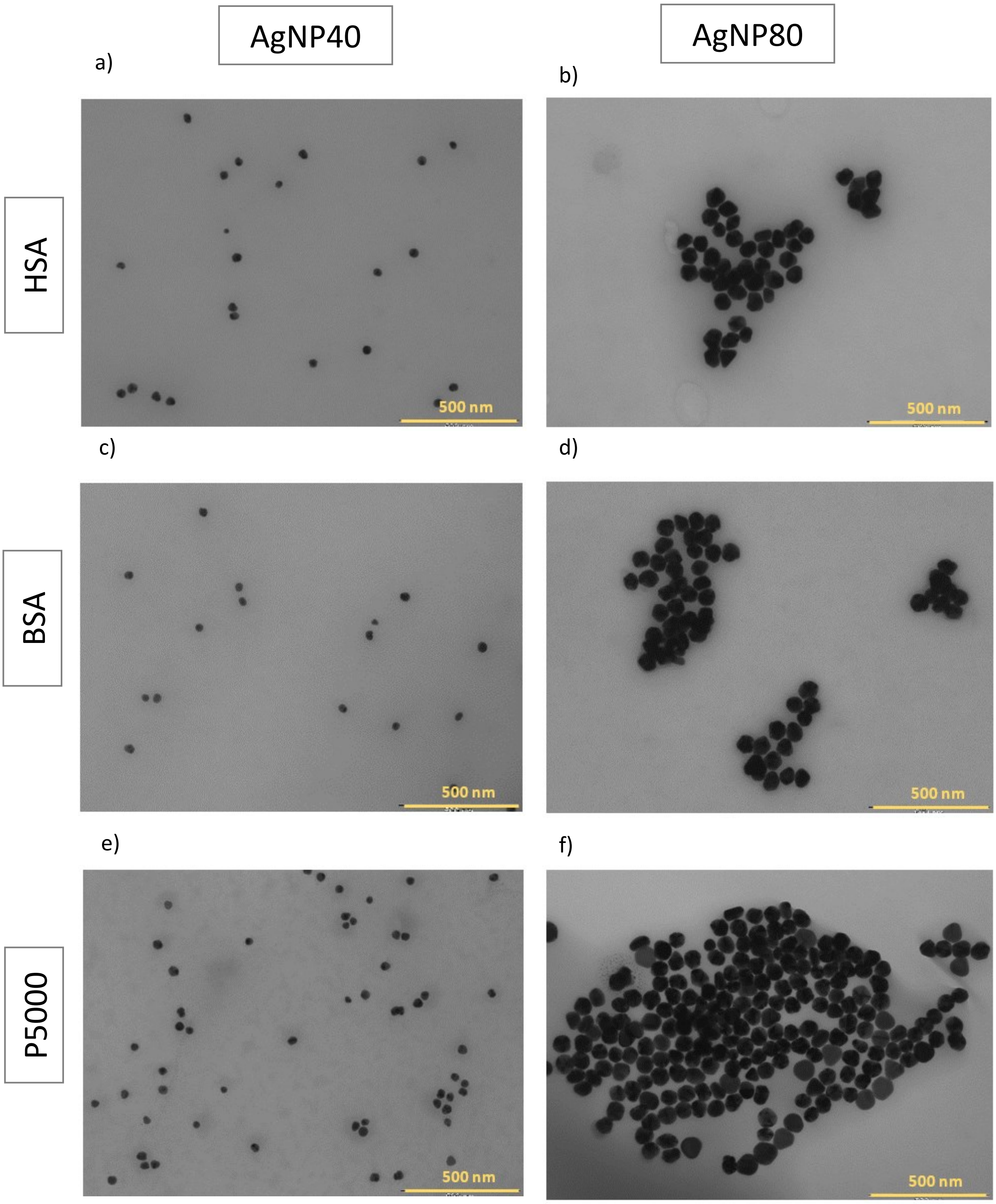

Figure 25 *Representative TEM images of AgNP40 and AgNP80 with different coatings. a) AgNP40_HSA; b) AgNP80_HSA; c) AgNP40_BSA; d) AgNP80_BSA; e) AgNP40_P5000; f) AgNP80_P5000*

Table 2 *UV-Vis, TEM and DLS data of AgNP40 pristine and with coatings (HSA, BSA and P5000)*

	AgNP40			
Sample	**Pristine**	**HSA**	**BSA**	**P5000**
λ_{max} (nm)	425	427	429	429
Extinction*	7.38	6.78	6.69	7.15
Size TEM[§] (nm)	33 (±11)	37 (±1)	31 (±5)	39 (±8)
Z average (nm)	62 (±9)	76 (±5)	67 (±5)	66 (±2)
Size in intensityˆ (nm)	55.3 (±0.9)	80 (±4)	71 (±3)	67 (±2)
Size in numberˆ (nm)	35 (±2)	49 (±6)	43 (±1)	41 (±1)
Pdiˆ	0.20 (±0.02)	0.11 (±0.02)	0.12 (±0.01)	0.12 (±0.01)
Normalized intensityˆ (kcps) 10^4	3.93 (±0.08)	3.99 (±0.02)	3.70 (±0.02)	3.500 (±0.005)
Zeta potential (mV)	-46 (±2)	-21 (±2)	-21 (±1)	-15 (±2)

Table 3 *UV-Vis, TEM and DLS data of AgNP80 pristine and with coatings (HSA, BSA and P5000)*

	AgNP80			
Sample	**Pristine**	**HSA**	**BSA**	**P5000**
λ_{max} (nm)	458	438	447	461
Extinction*	11.60	3.26	3.76	9.02
Size TEM[§] (nm)	78 (±13)	72 (±21)	78 (±28)	73 (±16)
Z average (nm)	79 (±4)	170 (±5)	134 (±12)	80 (±1)
Size in intensityˆ (nm)	97 (±3)	185 (±13)	148 (±5)	117 (±2)
Size in numberˆ (nm)	40 (±20)	125 (±9)	80 (±10)	62 (±2)
Pdiˆ	0.18 (±0.01)	0.19 (±0.03)	0.22 (±0.02)	0.123 (±0.005)
Normalized intensityˆ (kcps) 10^5	1.180 (±0.007)	3.39 (±0.06)	4.53 (±0.8)	5.0 (±0.1)
Zeta potential (mV)	-48 (±2)	-25 (±1)	-27 (±1)	-15 (±2)

**Corrected for the dilution factor*

[§] *Diameter and std dev calculated over 100 particles*

ˆDetermined at the backscatter angle (173°)

Each value is the average of three repeats. Values are reported as mean (±std dev)

Following the functionalisation with the three chosen coatings (HSA, BSA and P5000), the silver nanoparticles obtained were put through a second round of characterisation to establish if the functionalisation was successful, and how the different parameters could change with respect to the pristine nanoparticles.

UV-Vis spectra showed values of λ_{max} for covered AgNP40 that redshifted with respect to the spectra of pristine AgNP40, suggesting the successful functionalisation that also yielded larger particle sizes for all of the three coatings. As for AgNP80, values of λ_{max} varied from 438 up to 461 nm, and the spectra proved to be less symmetrical, showing a shoulder to the right of the main peak (fig.21a-f).

TEM analysis performed on these samples demonstrated that the silver core for both AgNP40 and AgNP80 remained unchanged. This result was reassuring, since the functionalisation was foreseen to form a molecular shell onto the particle's surface, undetectable by standard electron transmission microscopy (fig.22a-f).

As routinely done for the bare NPs, MADLS measurements were also carried out for the coated particles.

The characteristic size values, including Z average, size in intensity and size in number, showed a similar trend for coated AgNP40 and AgNP80: the size parameters increased after functionalisation, yet the observed increase was significantly higher for HSA, (i.e. Z average values of 170 (±5) nm for HSA and 134 (±12) nm for BSA vs 80 (±1) nm for P5000).

As can be inferred from DLS size distribution curves (fig.20a, c, e and 21a, c, e), the populations for both particle sizes and every surface functionalisation remained monodispersed, with low PDI values.

Additionally, the Z potential obtained on the six types of samples showed a decrease after functionalisation (in the range from -15 to -27 mV, versus the -45 mV of the pristine particles), though the negative values were enough to preserve particles stability.

UV-Vis spectra and DLS size distribution of the particles functionalised with the four additional PEG capping agents can be consulted in the Annexes A1 & A2, including tables with characteristic values in Annex A3 & A4.

The maximum intensity in the UV-Vis spectra were reached at wavelengths around 430-440 nm for AgNP40, while experimented a redshift for the bigger AgNP80, moving to approximately 500-530 nm.

Both particle populations for AgNP40 and AgNP80 samples showed an expected increase in size as the length of the PEG coating increased, varying in a range of 55 to 139 nm for AgNP40, and 300 to 350 nm for AgNP80.

Most importantly, the low values of PDI (<0.5) confirmed that also these populations of NPs were monodispersed in size.

3.3. Stability of the nanoparticles over time

The stability of key properties of the functionalised particles was assessed over a relatively long period of time. The particles investigated were, specifically: AgNP40_HSA, AgNP40_BSA, AgNP40_P5000 and AgNP80_HSA, AgNP40_BSA, AgNP40_P5000.

The time points chosen for stability measurements were two hours, four hours, twenty-four hours and four months. The main properties monitored were: (i) size in intensity and (ii) normalised intensity evaluated by MADLS analysis, while (iii) λ_{max} and (iv) extinction at the maximum of the peak using UV-vis spectrophotometer, reported in fig. 23 and 24 and Annex 5.

AgNP40

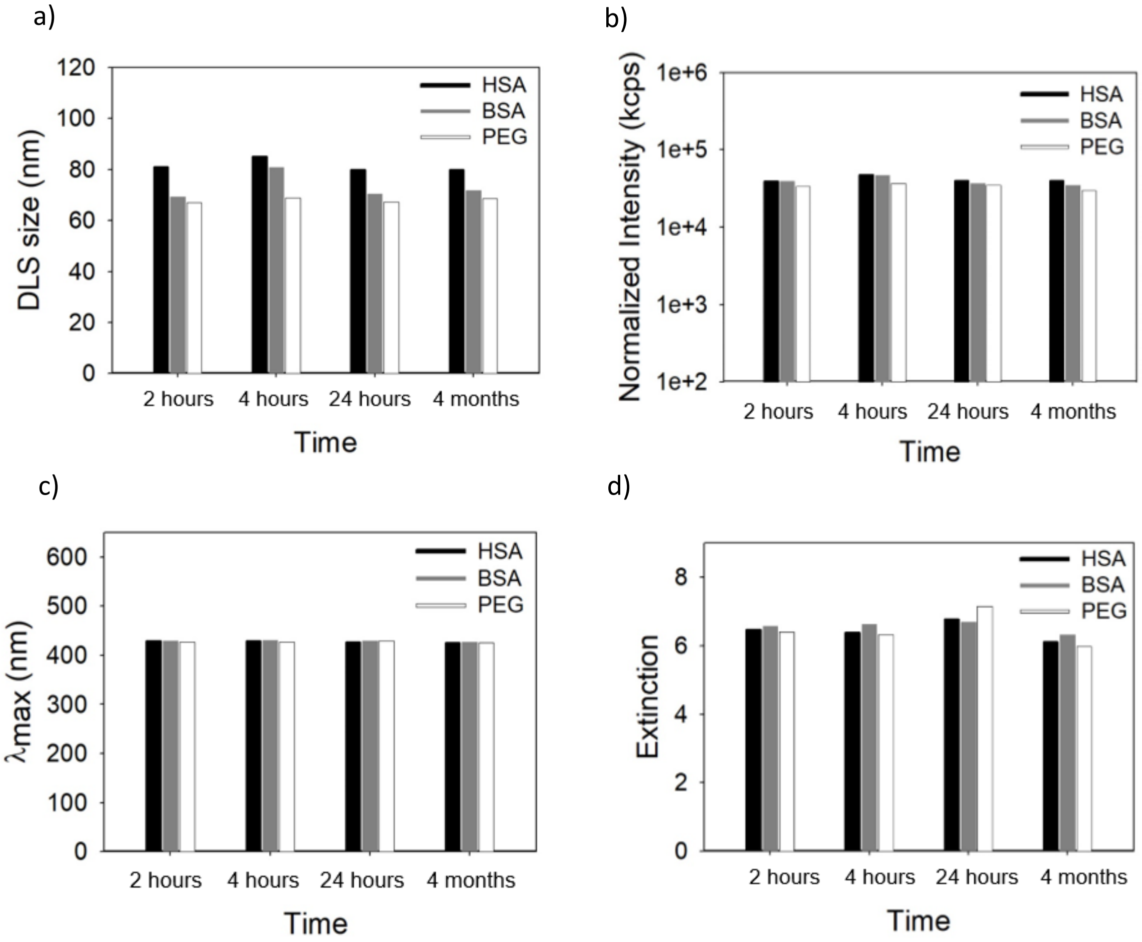

Figure 26 *Stability of AgNP40_HSA, AgNP40_BSA and AgNP40_P5000 at different time points. a) size* in intensity; b) normalized intensity*; c) UV-Vis λmax; d) optical extinction at λmax. *Each value is the average of three repeats and determined at the backscatter angle (173°)*

AgNP80

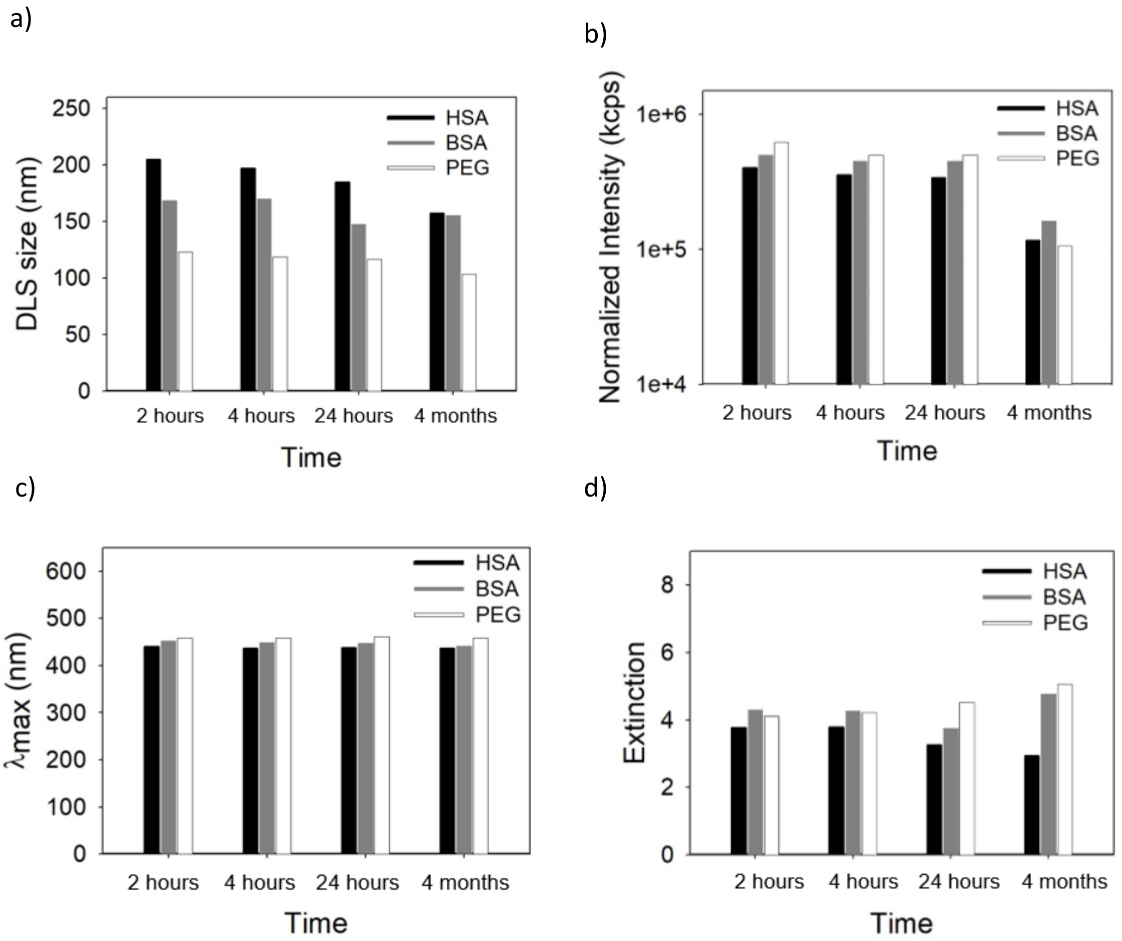

Figure 27 *Stability in time of AgNP80_HSA, AgNP80_BSA and AgNP80_P5000 a) size* in intensity; b) normalized intensity*; c) UV-Vis* λ_{max}*; d) optical extinction at* λ_{max}*. *Each value is the average of three repeats and determined at the backscatter angle (173°).*

From the results presented in Figure 23 and 24 it is possible to rationalize the trend of the DLS size for the six different types of nanoparticles as a function of time. Overall, all the particles were stable up to four months, without displaying tendency to aggregation. AgNP80 tend to precipitate over time, however the colloid was completely redispersed by vigorous vortexing.

AgNP40_P5000 showed the smaller variation of particle size, ranging from 67 (±2) to 69 nm (±2)). Conversely, AgNP40_HSA and AgNP40_BSA displayed fluctuations in particle size, that reached a plateau at longer time points.

In the case of AgNP80, the size varied slightly over time. For example, in the case of AgNP80_HSA it changed from 205 (±4) nm at 2 hours, to 158 (±27) measured after 4 months. A similar behaviour was also observed for AgNP80_BSA and AgNP80_P5000.

Normalised intensity values, which refers to the intensity of light scattered by the particles in the sample normalized against the instrument attenuation factor at the backscatter angle (173°), showed a stable value in time for AgNP40 with all three coatings, whereas in the case of AgNP80 the value decreased for the three coatings, going from over $4 \cdot 10^5$ kcps to a range between 1.07 and $1.62 \cdot 10^5$ kcps. This decrease in the normalised intensity is consistent with reduction in particle size mentioned above, or could be related to a decrease in particle concentration.

The bar plotting for λ_{max} provides the most stable scenario, with stationary values for both AgNP40 (between 425 and 429 nm) and AgNP80 (between 436 and 461 nm). This positive result can be interpreted as an evidence of stability, with no evidence of aggregation that will modify the LSPR wavelength.(19)

We observed higher variability for the extinction at the maximum wavelength. In fact, for AgNP80_HSA the extinction grew systematically smaller over time (from 3.76 to 2.93), whereas it went in the opposite direction for AgNP80_BSA and AgNP80_P5000 (from 4.30 to 4.77 for BSA and from 4.11 to 5.06 for P5000).

These contrasting results cannot be explained with a single rationale. The decrease in extinction values may be related to a reduction in the concentration of the NPs over time, possibly due to the precipitation phenomenon observed. Conversely, an increase in optical extension may be explained by evaporation of the solvent over time, due to inefficient seal of the sample container by human error. In the case of AgNP40, extinction values remained more stable, in the range between 6.78 and 6.11 for AgNP40_HSA, 6.69 and 6.31 for AgNP40_BSA, 5.98 and 7.15 for AgNP40_P5000.

The long-term stability at different time points was also assessed by UV-Vis spectroscopy for AgNP40 and AgNP80 with the other four coatings (P750, P6000, P10000, P20000). Values can be found in Annex 5.

On the other hand, the DLS size in intensity remained stable for all AgNPs with the different coatings, showing a small decrease in the case of AgNP40_P10000 (from 127 (±2) to 116 (±2) nm) and AgNP40_P20000 (from 136.4 (±0.9) to 116 (±2) nm) after four weeks, whereas the bigger particles displayed an opposite trend. In fact, AgNP80_P6000 and AgNP80_P20000 exhibited an increase as the time passed, going from 167 (±14) to 183 (±29) nm and from 175 (±10) to 199 (±32) respectively.

Normalised intensity tended to decrease over time for all AgNP40 although remaining in the same order of magnitude (10^5 kcps). The opposite behaviour was detectable for AgNP80, whose intensity increased, still remaining in the same order of magnitude (10^5 kcps) as well.

Maximum LSPR wavelength is the property that proved to be the most stable of all, showing little to no variation for all the combinations of AgNPs and coating agents, confirming the stability of these materials.

Extinction values remained unchanged, except for AgNP80_P6000 that anomalously changed from 4.19 to 6.41 over the course of four weeks, and for AgNP80_P20000 that passed from 4.95 at zero hours to 8.63 after four weeks, possibly due to variations in the particles concentration, as discussed above. These fluctuations on the AgNPs properties will be investigated in more detail in future work. However, for the scope of this Thesis, we can conclude that the particles were stable over time, opening to the possibility of using them as calibration materials for AF4 method development in the following section.

3.4. AF4 Method development

3.4.1. Effect of AF4 elution program

Silver nanoparticles of 40 and 80 nm coated with HSA, BSA and P5000 were chosen as model samples to develop a fractionation method using Asymmetrical Flow Field Flow Fractionation (AF4).

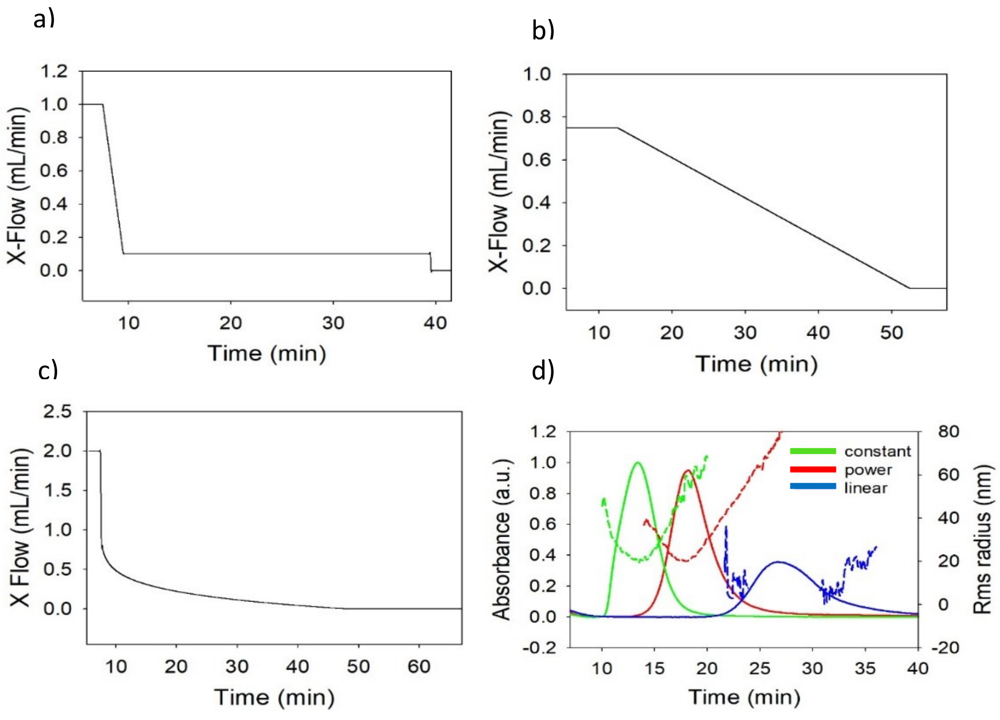

Figure 28 *Comparison between three different AF2000 elution programs. The first 5 to 10 min correspond to the focalisation step. a) XF0.1_constant elution program profile; b) XF0.75_linear gradient elution program profile; c) XF2_power gradient elution program profile; d) application of the three different elution programs to the same sample, AgNP40_HSA*

Table 4 UV peak area and retention time (Ret time) of AgNP40_HSA eluted with different AF4 elution programs.

	UV peak area (AU min) $\cdot 10^{-2}$	**Ret time* (min)**
XF0.1_constant	8.36	13.4
XF2_power	9.17	18.2
XF0.75_linear	5.84	26.6

**the time required for a particular analyte or particle to travel through the AF4 channel and reach the detector after being injected into the system*

The system used for the analysis of these NPs included a standard FFF channel and a regenerated cellulose membrane with a molecular weight cut-off of 10kDa. The spacer was 350 µm thick using the eluent phase NovaChem® 0.0125% v/v, as described in Materials and Methods section. As mentioned above, three coatings for AgNPs were chosen because they were stable and yielded negatively charged particle at physiological pH, ensuring repulsion from the negatively charged membrane.

The main objective of this piece of work was the selection of the optimal AF4 elution program, suitable to obtain efficient fractionation of the coated AgNPs with high analytical recoveries.

Initially, a constant cross flow method at a cross-flow rate of 0.1 mL/min was tested. In this case, the fractogram showed an intense and symmetrical peak (fig.25d, green plot) after 13.4 minutes. The distribution of Rms radius was also well defined, represented by the dotted green line. Since the peak eluted close to the FFF void peak (which represents the elution of non-retained particles or molecules that interact poorly with the separation field), a second elution program involving a linear gradient was tested, to move the peak at higher retention time and improve separation.

As a result, with the second method, the peak shifted from 13.4 to 26.6 min, but decreased considerably in intensity (from $8.36 \cdot 10^{-2}$ a.u. to $5.84 \cdot 10^{-2}$ a.u.) and the scattered light could not be fitted correctly by models to calculate Rms radius distribution (blue dotted line).

A third elution program was implemented, exploiting a power gradient from a cross flow rate of 2 mL/min to 0 mL/min with a decay parameter of 0.1. This elution program provided the best separation without compromising the analytical recovery, in fact the peak eluted at retention time between the two previous programs (18.2 min) and showed the highest intensity ($9.17 \cdot 10^{-2}$ a.u.) with a symmetrical shape. For these reasons we used the power decay method for further development within the following sections.

3.4.2. Effect of particles size

After selecting the optimal AF4 method (XF2_power), two different sets of NPs were analysed (AgNP40_HSA and AgNP80_HSA) to compare the same method on similar particles with different sizes.

The fractionation of both samples using the XF2_power program was successful. The retention times shifted from 18.2 min to 29.8 min for AgNP40_HSA and

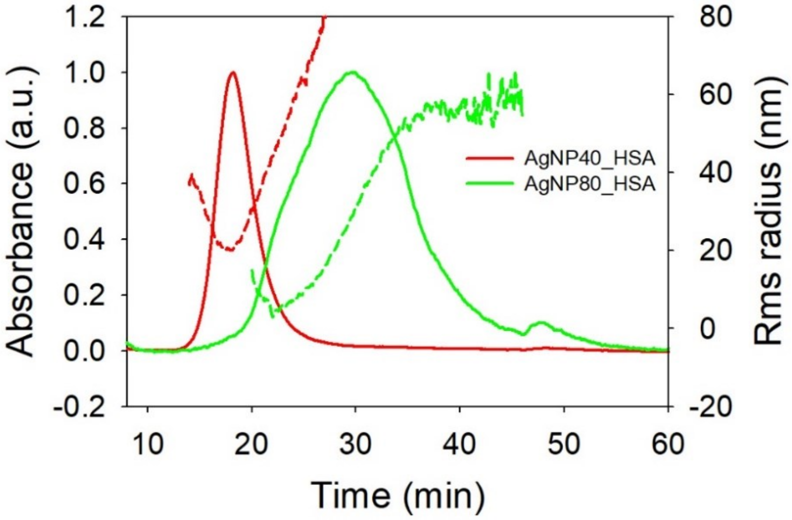

Figure 29 *Characterisation of particles of different size - application of the same elution program, XF2_power, to AgNP40_HSA and AgNP80_HSA. The peaks were normalised to better show their shape*

AgNP80_HSA, respectively. This result is consistent with the difference in size for these two types of particles.

Table 5 *Comparison between characteristic parameters of AgNP40_HSA and AgNP80_HSA*

	AgNP40_HSA	**AgNP80_HSA**
UV peak area (AU min) $\cdot 10^{-2}$	9.17	4.20
Ret time (min)	18.2	29.8
Rn (nm)	26 (±3)	54 (±5)
Rw (nm)	32 (±2)	69 (±4)
Rz (nm)	55 (±2)	76 (±4)
PDI (st)	1.57	1.61

The three values of radius extracted from the MALS measurements using the software ASTRA were: Rz that refers to the z-average radius of gyration, Rn that refers to the number-average radius of gyration, and Rw that refers to the mass weighted radius of gyration. The slight differences between the three radiuses obtained for the same sample depend on the way the parameters are calculated and may reflect the effect of anisotropy or polydispersity.

The particle radius for both AgNP40 and AgNP80 are consistent with the size obtained from batch MADLS measurements (Tab.3), confirming that the fractionation method is not affecting the average properties of the sample, while effectively separating the monomodal particle population as a function of size.

One more information to take into account is that static polydisperse index PDI(st) calculated from MALS is different from dynamic PDI calculated from DLS data. PDI(st) is calculated as the ratio between $(Rw)^2$ and $(Rn)^2$ and therefore can take values higher than 1.

The symmetry, narrowness and low static PDI of the peak for AgNP40_HSA reflects the monodispersity of the sample. Although showing a wider peak, the population of AgNP80_HSA results monodisperse as well, given its low static PDI value.

Uncertainties for the size parameters were below 5%, reflecting the reliable performance of the numerical fitting of the data.

From the data presented in this section we can conclude that the power method efficiently fractionated particles in a wide range of particle sizes and that these materials can be efficiently used for the optimization of AF4 methods and as potential calibration test materials to determine particle size using AF4 retention times.

3.4.3. Effect of particle surface functionalisation (HSA, BSA, P5000)

Another comparison with the same AF4 method was carried out among particles of the same size, but with different surface coatings. Particularly, AgNP40 with three coatings (HSA, BSA, P5000) were chosen.

In Figure 27 we report representative AF4 peaks for the three sample types. These peaks are symmetric and narrow, indicating monodisperse populations of particles. This is also confirmed by low PDI(st) values in Table 6.

It is possible to observe that retention times are in line with the expected size from DLS in batch. In fact, AgNP40_HSA, which were believed to be the biggest particles from DLS values shown in Tab. 2 (Z Average 76 (±5) nm), exhibit a value of retention time (18.2 min) higher than the ones of AgNP40_BSA and AgNP40_P5000.

Even the values of radiuses obtained from MALS measurements for this sample confirm that AgNP40_HSA are bigger than AgNP40_P5000.

On the other hand, AgNP40_BSA show the highest values of radius amongst all three samples, even though they eluted first. This can be due to a different interaction of their coating with the membrane-carrier system, leading to a different retention behaviour inside the channel. Retention time may also vary with membrane conditioning, aging of the membrane, and history of samples measured before. Since this phenomenon cannot be fully rationalized based on data available, further experiments will be scheduled as future work to clarify this anomaly.

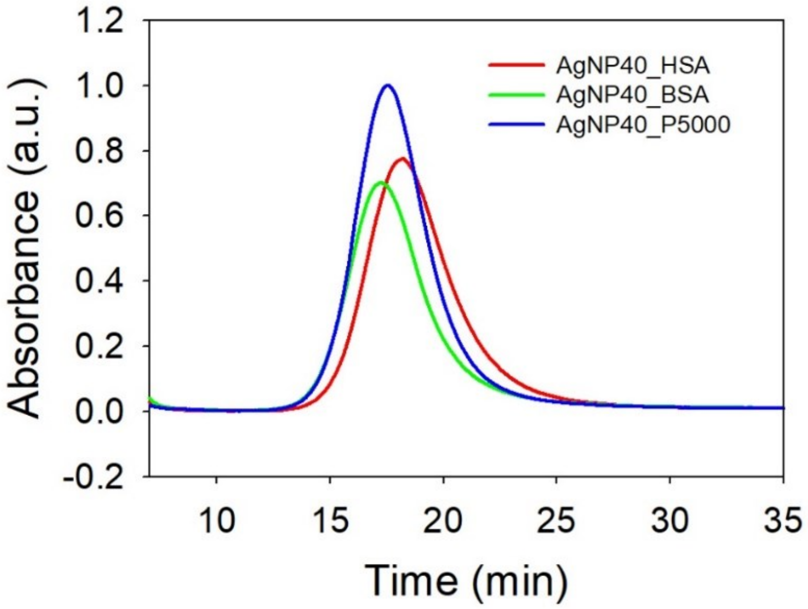

Figure 30 *Change of particles functionalisation; application of the same elution program, XF2_power, to AgNP40_HSA, AgNP40_BSA and AgNP40_P5000*

Table 6 Comparison between AF2000 data of AgNP40_HSA, AgNP40_BSA and AgNP40_P5000

	AgNP40_HSA	**AgNP40_BSA**	**AgNP40_P5000**
UV peak area (AU min) ·10^{-2}	9.18	7.75	10.28
Ret time (min)	18.2	17.2	17.5
Rn (nm)	26 (±3)	38 (±1)	15 (±31)
Rw (nm)	32 (±2)	43 (±1)	21 (±20)
Rz (nm)	55 (±2)	56 (±1)	37 (±10)
PDI(st)	1.57	1.25	1.92

4. Conclusions

The work presented in this thesis has led to the accomplishment of its original objectives. We successfully found two distinct reliable procedures for the synthesis of silver nanoparticles (AgNPs) of a desired size, in particular a reduction of AgNO3 by means of tannic acid to obtain AgNPs of 40 nm, and a “seed-growth” method starting from AgNP40 as seeds to obtain AgNPs of approximately 80 nm. These pristine NPs were characterised using DLS, UV-Vis and TEM imaging, and all the results confirmed the size expected from the synthesis procedures developed.

It was also possible to demonstrate the monodisperse character of the colloidal solutions obtained, reflected in the narrow shape of UV-Vis peaks and the low PDI values obtained by MADLS. The stability in solution of these NPs was ensured by the negative values of Zeta Potential.

The second aim of the work was the functionalisation of the pristine NPs with some coating agents, including two model proteins (HSA and BSA) and five different polyethylene glycol of specific chain lengths (P750, P5000COOH, P6000, P10000, P20000).

The functionalisation procedure devised after several optimization trials was successful and provided AgNPs with an organic coating which were foreseen suitable to be used as reference test samples to develop fractionation methods using the AF4 technique at a later stage.

To assess if the functionalisation was successful and to determine how the different parameters would change with respect to the pristine nanoparticles, the coated AgNPs were further characterised.

Overall, the values obtained from DLS, UV-Vis and TEM imaging showed an increase in size after the functionalisation, confirming that the formation of a shell of coating material had occurred on the surface of the metallic core of the

NPs. Key parameters, including PDI and Zeta Potential, remained almost unvaried, proving that the AgNPs were not affected by the functionalisation. These functionalised NPs were subjected to a stability test over time up to four months.

The parameters monitored (normalised size and intensity at MADLS, λmax and extinction at the peak maximum at UV-Vis) showed some fluctuations over time although displaying a stable trend. The fluctuations in the properties of AgNPs will be analysed in more detail in future work. However, for the purpose of this thesis, we can conclude that the particles remained stable over time, opening to the possibility of using them as calibration materials for the development of the AF4 method in the final part of the thesis.

The analyses performed by Asymmetrical Flow Field-Flow Fractionation (AF4) confirmed this technique as an effective method for fractionating and characterizing silver nanoparticles, especially when coupled with multiple detectors (MALS, UV-Vis, dRI).

The AF4 elution program involving a power gradient with a decay rate of 0.1 was the most efficient for the fractionation of particles in a wide range of sizes. This method was particularly successful in distinguishing particles bearing the same coating agent but with a metallic core of different size (AgNP40_HSA and AgNP80_HSA,) suggesting that the materials could be efficiently used for the optimization of AF4 methods and as potential calibration test materials to determine particle size using AF4 retention times.

While AF4 was effective in distinguishing particles with metallic cores of different sizes, some unexpected anomalies were observed, particularly when comparing radius measurements of AgNP40 with three different coatings, namely HSA, BSA and P5000. In fact, AgNP40_BSA showed an unexpected behaviour, providing radius values by MALS which were not in line with retention times obtained nor with the previously acquired DLS measurements.

5. Future work

The discrepancies highlighted during AF4 data elaboration suggest the need for further investigation to fully understand the behaviour of functionalized nanoparticles in the AF4 system. Further experiments should be conducted to explore the unexpected anomalies observed in the AF4 radius values of BSA-coated silver nanoparticles (AgNPs). Understanding these discrepancies will be crucial for improving the accuracy of nanoparticle characterization using AF4.

If an explanation for these anomalous behaviours is found, it will be possible to extend the range of functionalisation agents beyond the current selection of proteins and PEGs to include other biocompatible and functional molecules.

This could provide a broader understanding of how different coatings impact nanoparticle stability, functionality, and behaviour in biological environments.

Another interesting point would be the spiking of the particles in complex biological matrices, to test the efficiency of the AF4 fractionation in a physiologically relevant medium.

Regarding the characterisation in batch of the AgNPs and the study of stability, it will be essential to conduct more extensive long-term stability monitoring on functionalized AgNPs under various environmental conditions. This will help to assess their reliability as reference test materials.

Keeping in mind these objectives for future studies, it is possible to conclude that AgNPs were successfully synthesised and functionalised, and that it will be possible to employ them as reference materials for future studies, particularly for the optimization of AF4 methods for nanoparticle characterization. The stability of these particles opens up possibilities for their use in various applications, including calibration materials.

6. Annexes

AgNP40

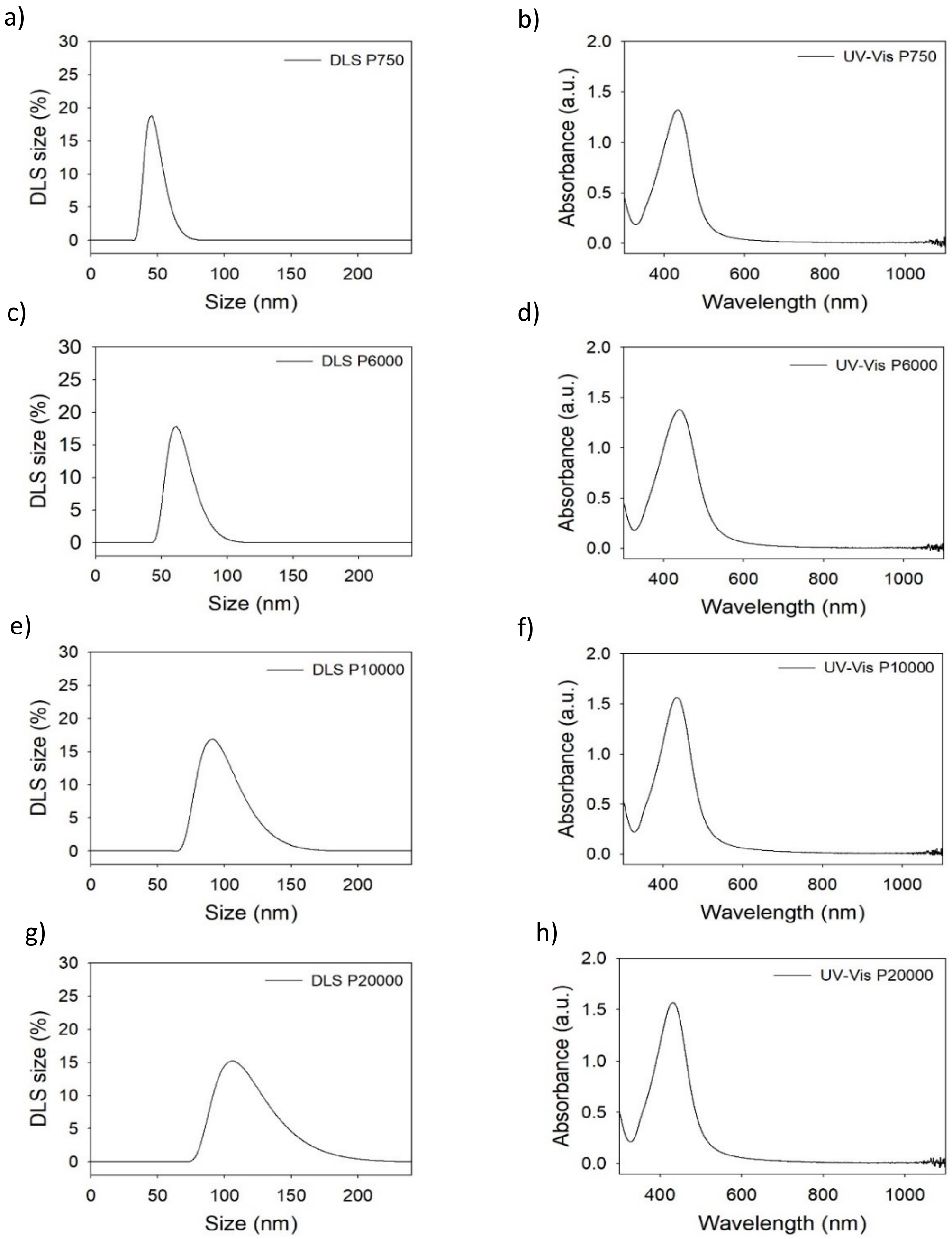

Annex 1. *General characterisation of AgNP40 with different coatings a) representative MADLS size distribution by number of AgNP40_P750; b) representative UV-Vis spectra of AgNP40_P750; c) representative MADLS size distribution by number of AgNP40_P6000; d) representative UV-Vis spectra of AgNP40_P6000; e) representative MADLS size distribution by number of AgNP40_P10000; f) representative UV-Vis spectra of AgNP40_P10000; g) representative MADLS size distribution by number of AgNP40_P20000; h) representative UV-Vis spectra of AgNP40_P20000*

AgNP80

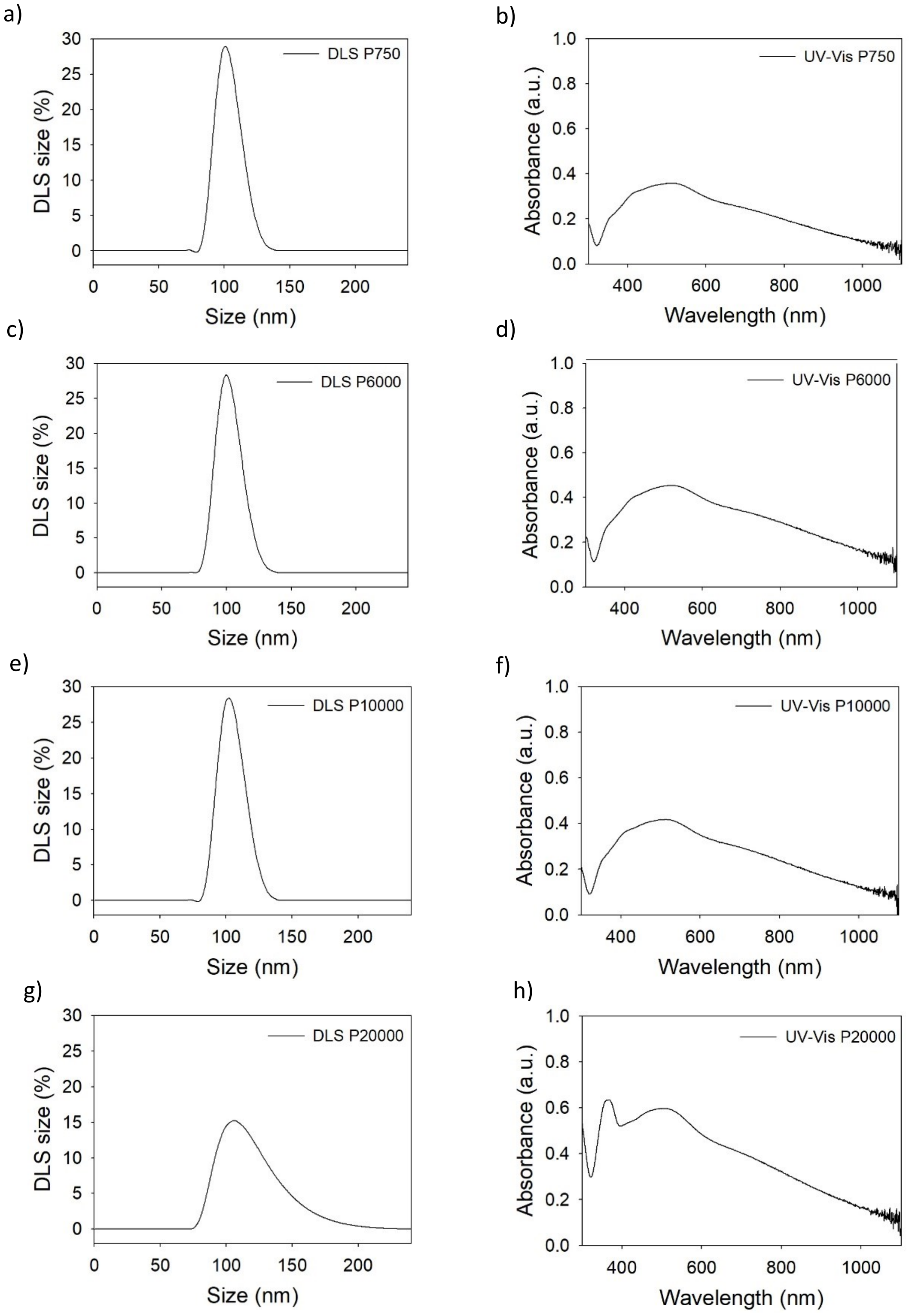

Annex 2. *General characterisation of AgNP80 with different coatings a) representative MADLS size distribution by number of AgNP80_P750; b) representative UV-Vis spectra of AgNP80_P750; c) representative MADLS size distribution by number of AgNP80_P6000; d) representative UV-Vis spectra of AgNP80_P6000; e) representative MADLS size distribution by number of AgNP80_P10000; f) representative UV-Vis spectra of AgNP80_P10000; g) representative MADLS size distribution by number of AgNP80_P20000; h) representative UV-Vis spectra of AgNP80_P20000*

Annex 3. *UV-Vis and DLS data of AgNP40 pristine and with coatings P750, P6000, P10000 and P20000)*

	AgNP40			
Sample	***P750***	***P6000***	***P10000***	***P20000***
λ_{max} (nm)	435	441	435	432
Extinction*	3.97	4.14	4.70	4.71
Z average (nm)	55 (±3)	76 (±4)	115 (±8)	139 (±7)
Size in intensityˆ (nm)	61 (±2)	83 (±2)	125 (±4)	143 (±6)
Size in numberˆ (nm)	39.5 (±5)	51 (±2)	70 (±7)	87 (±6)
Pdiˆ	0.16 (±0.01)	0.10 (±0.01)	0.11 (±0.01)	0.14 (±0.01)
Normalized intensityˆ (kcps)$\cdot 10^4$	8.36 (±0.02)	12.50 (±0.08)	14.50 (±0.09)	10.67 (±0.06)

Annex 4. *UV-Vis and DLS data of AgNP80 pristine and with coatings P750, P6000, P10000 and P20000)*

	AgNP80			
Sample	***P750***	***P6000***	***P10000***	***P20000***
λ_{max} (nm)	515	527	511	500
Extinction*	1.07	1.36	1.25	1.79
Z average (nm)	325 (±56)	341 (±62)	354 (±109)	305 (±49)
Size in intensityˆ (nm)	144 (±7)	171 (±13)	188 (±3)	189 (±23)
Size in numberˆ (nm)	134 (±3)	159 (±5)	176 (±24)	174 (±8)
Pdiˆ	0.33 (±0.07)	0.36 (±0.04)	0.40 (±0.06)	0.38 (±0.08)
Normalized intensityˆ (kcps) $\cdot 10^5$	1.05 (±0.04)	1.43 (±0.04)	1.25 (±0.06)	1.69 (±0.04)

**Corrected for the dilution factor*
ˆDetermined at the backscatter angle (173°)
Each value is the average of three repeats. Values are reported as mean (±std dev)

Annex 5. *Stability in time of AgNP40 and AgNP80 pristine and with 7 coatings (HSA, BSA, P750, P5000, P6000, P10000, P20000)*

AgNP40_HSA	**Size in intensityˆ (nm)**	**Normalized intensityˆ (kcps) $\cdot 10^4$**	**λ_{max} (nm)**	**Extinction***
2 hours	81 (±3)	3.93 (±0.02)	429	6.48
4 hours	85 (±2)	4.77 (±0.08)	429	6.39
24 hours	80 (±4)	3.99 (±0.02)	427	6.78
4 months	79 (±4)	3.99 (±0.02)	426	6.11

AgNP40_BSA	**Size in intensityˆ (nm)**	**Normalized intensity (kcps)ˆ $\cdot 10^4$**	**λ_{max} (nm)**	**Extinction***
2 hours	69 (±2)	3.93 (±0.03)	429	6.56
4 hours	81 (±2)	4.690 (±0.007)	430	6.62
24 hours	71 (±3)	3.70 (±0.02)	429	6.69
4 months	72 (±1)	3.52 (±0.02)	427	6.31

AgNP40_P5000	**Size in intensityˆ (nm)**	**Normalized intensity (kcps)ˆ $\cdot 10^4$**	**λ_{max} (nm)**	**Extinction***
2 hours	67 (±2)	3.382 (±0.004)	427	6.40
4 hours	69 (±5)	3.66 (±0.096)	427	6.31
24 hours	67 (±2)	3.502 (±0.005)	429	7.15
4 months	68.5 (±0.4)	2.972 (±0.004)	425	5.98

AgNP80_HSA	**Size in intensityˆ (nm)**	**Normalized intensity (kcps)ˆ $\cdot 10^5$**	**λ_{max} (nm)**	**Extinction***
2 hours	205 (±4)	4.01 (±0.04)	440	3.76
4 hours	197 (±13)	3.55 (±0.02)	437	3.78
24 hours	185 (±13)	3.39 (±0.06)	438	3.26
4 months	158 (±27)	1.17 (±0.02)	436	2.93

AgNP80_BSA	**Size in intensityˆ (nm)**	**Normalized intensity (kcps)ˆ $\cdot 10^5$**	**λ_{max} (nm)**	**Extinction***
2 hours	169 (±18)	5.00 (±0.09)	452	4.30
4 hours	170 (±16)	4.51 (±0.09)	449	4.26
24 hours	148 (±5)	4.53 (±0.08)	447	3.76
4 months	155 (±16)	1.62 (±0.05)	441	4.77

AgNP80_P5000	**Size in intensityˆ (nm)**	**Normalized intensity (kcps)ˆ $\cdot 10^5$**	**λ_{max} (nm)**	**Extinction***
2 hours	123.2 (±0.3)	6.22 (±0.05)	459	4.11
4 hours	119 (±4)	4.99 (±0.04)	459	4.22
24 hours	117 (±2)	5.0 (±0.1)	461	4.51
4 months	103.7 (0.5)	1.07 (±0.01)	459	5.06

AgNP40_P750	**Size in intensity^ (nm)**	**Normalized intensity (kcps)^ ·10^4**	**λ_{max} (nm)**	**Extinction***
0 hours	60.9 (±0.9)	10.3 (±0.1)	433	4.32
24 hours	61 (±2)	8.36 (±0.02)	434	3.97
1 week	62 (±3)	8.96 (±0.04)	434	3.58
4 weeks	63 (±1)	9.08 (±0.05)	433	4.12

AgNP40_P6000	**Size in intensity^ (nm)**	**Normalized intensity (kcps) ^ ·10^5**	**λ_{max} (nm)**	**Extinction***
0 hours	74.5 (±0.7)	1.30 (±0.01)	435	5.24
24 hours	83 (±2)	1.252 (±0.008)	435	4.11
1 week	88 (±2)	1.369 (±0.004)	434	4.37
4 weeks	85.7 (±0.7)	1.14 (±0.01)	434	4.08

AgNP40_P10000	**Size in intensity^ (nm)**	**Normalized intensity (kcps)^ ·10^5**	**λ_{max} (nm)**	**Extinction***
0 hours	127 (±2)	2.8 (±0.1)	436	4.80
24 hours	125 (±4)	1.453 (±0.009)	436	4.69
1 week	125 (±5)	1.369 (±0.004)	436	4.90
4 weeks	116 (±2)	1.254 (±0.001)	434	4.88

AgNP40_P20000	**Size in intensity^ (nm)**	**Normalized intensity (kcps)^ ·10^5**	**λ_{max} (nm)**	**Extinction***
0 hours	136.4 (±0.9)	1.33 (±0.01)	432	4.71
24 hours	143 (±6)	1.067 (±0.006)	432	4.71
1 week	139 (±7)	1.266 (±0.003)	432	4.84
4 weeks	112 (±2)	1.132 (±0.006)	432	4.62

AgNP80_P750	Size in intensityˆ (nm)	Normalized intensity (kcps)ˆ $\cdot 10^5$	λ_{max} (nm)	Extinction*
0 hours	152 (±21)	1.07 (±0.01)	515	3.44
24 hours	144 (±7)	1.07 (±0.04)	515	3.58
1 week	147 (±19)	1.10 (±0.01)	515	3.63
4 weeks	141 (±7)	1.14 (±0.05)	513	3.55

AgNP80_P6000	Size in intensityˆ (nm)	Normalized intensity (kcps)ˆ $\cdot 10^3$	λ_{max} (nm)	Extinction*
0 hours	167 (±14)	1.25 (±0.06)	520	4.19
24 hours	171 (±13)	1.43 (±0.04)	520	4.54
1 week	172 (±15)	1.32 (±0.09)	522	5.02
4 weeks	183 (±29)	1.9 (±0.1)	521	6.41

AgNP80_P10000	Size in intensityˆ (nm)	Normalized intensity (kcps)ˆ $\cdot 10^5$	λ_{max} (nm)	Extinction*
0 hours	175 (±15)	1.24 (±0.01)	511	4.12
24 hours	188 (±36)	1.25 (±0.06)	511	4.17
1 week	173 (±13)	1.31 (±0.03)	511	4.14
4 weeks	173 (±22)	1.3 (±0.1)	510	4.52

AgNP80_P20000	Size in intensityˆ (nm)	Normalized intensity (kcps)ˆ $\cdot 10^5$	λ_{max} (nm)	Extinction*
0 hours	175 (±10)	1.45 (±0.03)	500	4.95
24 hours	189 (±23)	1.69 (±0.04)	500	5.97
1 week	191 (±18	2.53 (±0.03)	500	6.68
4 weeks	199 (±32)	3.1 (±0.2)	500	8.63

**Corrected for the dilution factor*

ˆEach value is the average of three repeats and determined at the backscatter angle (173°). Values are reported as mean (±std dev)

7. Table of abbreviations

NPs: nanoparticles

AgNPs: silver nanoparticles

AgNP40: 40 nm silver nanoparticles

AgNP80: 80 nm silver nanoparticles

TEM: transmission electron microscopy

MADLS: multi angle dynamic light scattering

AF4: asymmetrical flow field flow fractionation

MALS: multi angle light scattering

dRI: refractive index detector

XF: cross flow

PDI: polidispersity index

HSA: human serum albumin

BSA: bovine serum albumin

PEG: polyethylene glycol

P750: 750 Dalton polyethylene glycol

P5000/P5000COOH: 5000 Dalton carboxylated polyethylene glycol

P6000: 6000 Dalton polyethylene glycol

P10000: 10000 Dalton polyethylene glycol

P20000: 20000 Dalton polyethylene glycol

8. Bibliography

(1) Khan, I., Saeed, K., & Khan, I. (2019). Nanoparticles: Properties, applications and toxicities. *Arabian Journal of Chemistry* (Vol. 12, Issue 7, pp. 908–931)

(2) Ealias, A. M., & Saravanakumar, M. P. (2017). A review on the classification, characterisation, synthesis of nanoparticles and their application. *IOP Conference Series: Materials Science and Engineering*, *263*(3)

(3) AbdelHamid, A. A., Mendoza-Garcia, A., & Ying, J. Y. (2022). Advances in and prospects of nanomaterials’ morphological control for lithium rechargeable batteries, *Nano Energy* (Vol. 93)

(4) Almatroudi, A. (2020). Silver nanoparticles: Synthesis, characterisation and biomedical applications. In *Open Life Sciences* (Vol. 15, Issue 1, pp. 819–839)

(5) Hutter, E., & Fendler, J. H. (2004). Exploitation of localized surface plasmon resonance. *Advanced Materials*, *16*(19), 1685–1706

(6) Sevenler, D., Lortlar Ünlü, N., & Ünlü, M. S. (2015). Nanoparticle biosensing with interferometric reflectance imaging. In *Nanobiosensors and Nanobioanalyses* (pp. 81–95). Springer Japan

(7) Bean, C. P., & Livingston, J. D. (1959). Superparamagnetism. *Journal of Applied Physics*, *30*(4), S120–S129

(8) Ali, A., Zafar, H., Zia, M., ul Haq, I., Phull, A. R., Ali, J. S., & Hussain, A. (2016). Synthesis, characterization, applications, and challenges of iron oxide nanoparticles. In *Nanotechnology, Science and Applications* (Vol. 9, pp. 49–67)

(9) Wiechers, Johann W., Musee, N. (2010). Engineered Inorganic Nanoparticles and Cosmetics: Facts , Issues , Knowledge Gaps and Challenges. In *Journal of Biomedical Nanotechnology* (Vol. 6, Issue 5, pp. 408-431)

(10)Geiss, O., Cascio, C., Gilliland, D., Franchini, F., & Barrero-Moreno, J. (2013). Size and mass determination of silver nanoparticles in an aqueous matrix using asymmetric flow field flow fractionation coupled to inductively coupled plasma mass spectrometer and ultraviolet-visible detectors. *Journal of Chromatography A*, *1321*, 100–108

(11)Wei, L., Lu, J., Xu, H., Patel, A., Chen, Z. S., & Chen, G. (2015). Silver nanoparticles: Synthesis, properties, and therapeutic applications. In *Drug Discovery Today* (Vol. 20, Issue 5, pp. 595–601)

(12)Chang, Y. jie, Shih, Y. hsin, Su, C. H., & Ho, H. C. (2017). Comparison of three analytical methods to measure the size of silver nanoparticles in real environmental water and wastewater samples. *Journal of Hazardous Materials*, *322*, 95–104

(13)https://www.postnova.com/. [Online]

(14)Analytics®, Postnova 2015, AF2000 Series Software Manual V2.0.0.1.

(15)Martin E. Schimpf, Karin Caldwell, J. Calvin. 2000, FIELD-FLOW FRACTIONATION HANDBOOK, John Wiley & Sons, Inc.

(16)Wyatt Tehcnology Corporation 2014, Rappels sur la diffusion de lumiere

(17)Morris, G., Sorzabal-Bellido, I., Bilton, M., Dawson, K., McBride, F., Raval, R., Jäckel, F., & Diaz Fernandez, Y. A. (2021). A novel self-assembly strategy for the fabrication of nano-hybrid satellite materials with plasmonically enhanced catalytic activity. Nanomaterials, 11(6)

(18) Bastús, N. G., Merkoçi, F., Piella, J., & Puntes, V. (2014). Synthesis of highly monodisperse citrate-stabilized silver nanoparticles of up to 200 nm: Kinetic control and catalytic properties. Chemistry of Materials, 26(9), 2836–2846

(19) Amato, E., Diaz-Fernandez, Y. A., Taglietti, A., Pallavicini, P., Pasotti, L., Cucca, L., Milanese, C., Grisoli, P., Dacarro, C., Fernandez-Hechavarria, J. M., & Necchi, V. (2011). Synthesis, characterization and antibacterial activity against gram positive and gram negative bacteria of biomimetically coated silver nanoparticles. Langmuir, 27(15), 9165–9173